

## SIGNATURES OF HIERARCHICAL MERGERS IN BLACK HOLE SPIN AND MASS DISTRIBUTION

HIROMICHI TAGAWA<sup>1</sup>, ZOLTÁN HAIMAN<sup>2</sup>, IMRE BARTOS<sup>3</sup>, BENCE KOCSIS<sup>4</sup>, KAZUYUKI OMUKAI<sup>1</sup><sup>1</sup>Astronomical Institute, Graduate School of Science, Tohoku University, Aoba, Sendai 980-8578, Japan<sup>2</sup>Department of Astronomy, Columbia University, 550 W. 120th St., New York, NY, 10027, USA<sup>3</sup>Department of Physics, University of Florida, PO Box 118440, Gainesville, FL 32611, USA<sup>4</sup>Department of Physics, Oxford University*Draft version April 21, 2021*

## ABSTRACT

Recent gravitational wave (GW) observations by LIGO/Virgo show evidence for hierarchical mergers, where the merging BHs are the remnants of previous BH merger events. These events may carry important clues about the astrophysical host environments of the GW sources. In this paper, we present the distributions of the effective spin parameter ( $\chi_{\text{eff}}$ ), the precession spin parameter ( $\chi_p$ ), and the chirp mass ( $m_{\text{chirp}}$ ) expected in hierarchical mergers. Under a wide range of assumptions, hierarchical mergers produce (i) a monotonic increase of the average of the typical total spin for merging binaries, which we characterize with  $\bar{\chi}_{\text{typ}} \equiv \overline{(\chi_{\text{eff}}^2 + \chi_p^2)^{1/2}}$ , up to roughly the maximum  $m_{\text{chirp}}$  among first-generation (1g) BHs, and (ii) a plateau at  $\bar{\chi}_{\text{typ}} \sim 0.6$  at higher  $m_{\text{chirp}}$ . We suggest that the maximum mass and typical spin magnitudes for 1g BHs can be estimated from  $\bar{\chi}_{\text{typ}}$  as a function of  $m_{\text{chirp}}$ . The GW data observed in LIGO/Virgo O1–O3a prefers an increase in  $\bar{\chi}_{\text{typ}}$  at low  $m_{\text{chirp}}$ , which is consistent with the growth of the BH spin magnitude by hierarchical mergers, at  $\sim 2\sigma$  confidence. A Bayesian analysis using the  $\chi_{\text{eff}}$ ,  $\chi_p$ , and  $m_{\text{chirp}}$  distributions suggests that 1g BHs have the maximum mass of  $\sim 15\text{--}30 M_\odot$  if the majority of mergers are of high-generation BHs (not among 1g–1g BHs), which is consistent with mergers in active galactic nucleus disks and/or nuclear star clusters, while if mergers mainly originate from globular clusters, 1g BHs are favored to have non-zero spin magnitudes of  $\sim 0.3$ . We also forecast that signatures for hierarchical mergers in the  $\bar{\chi}_{\text{typ}}$  distribution can be confidently recovered once the number of GW events increases to  $\gtrsim O(100)$ .

**Keywords:** binaries: close – gravitational waves – black hole mergers – methods: data analysis – stars: black holes

## 1. INTRODUCTION

Recent detections of gravitational waves (GWs) by LIGO (Aasi et al. 2015) and Virgo (Acernese et al. 2015) have shown evidence for a high rate of black hole (BH)-BH and neutron star (NS)-NS mergers in the Universe (Abbott et al. 2019b; Venumadhav et al. 2019; Abbott et al. 2020b). However, proposed astrophysical pathways to mergers remain highly debated. Indeed there are currently a large number of such possible pathways, with widely different environments and physical processes. A possible list of these currently includes isolated binary evolution (e.g. Dominik et al. 2012; Kinugawa et al. 2014; Belczynski et al. 2016; Spera et al. 2019) accompanied by mass transfer (Pavlovskii et al. 2017; Inayoshi et al. 2017; van den Heuvel et al. 2017), common envelope ejection (e.g. Paczynski 1976; Ivanova et al. 2013), envelope expansion (Tagawa et al. 2018), chemically homogeneous evolution in a tidally distorted binary (de Mink & Mandel 2016; Mandel & de Mink 2016; Marchant et al. 2016), evolution of triple or quadruple systems (e.g. Silsbee & Tremaine 2017; Antonini et al. 2017; Michaely & Perets 2019), gravitational capture (e.g. O’Leary et al. 2009; Gondán et al. 2018; Rasskazov & Kocsis 2019), dynamical evolution in open clusters (e.g. Banerjee 2017; Kumamoto et al. 2018; Rastello et al. 2019), young stellar clusters (e.g. Ziosi et al. 2014; Di Carlo et al. 2019; Rastello et al. 2020), and dense star clusters (e.g. Portegies Zwart & McMillan 2000; Samsing et al. 2014;

O’Leary et al. 2016; Rodriguez et al. 2016a), and interaction in active phases of galactic nucleus (AGN) disks (e.g. Bartos et al. 2017; Stone et al. 2017; McKernan et al. 2018; Tagawa et al. 2020b).

Recently several GW events were reported by LIGO and Virgo whose measured physical properties pose interesting constraints on their astrophysical origin. These include nine candidates for mergers in the upper-mass gap ( $\sim 50\text{--}130 M_\odot$ ) such as GW190521 (Abbott et al. 2019b; Zackay et al. 2019; Abbott et al. 2020b; The LIGO Scientific Collaboration et al. 2020b; Abbott et al. 2020c). Additionally, mergers with very unequal masses have been reported – GW190412 ( $q = 0.28^{+0.13}_{-0.07}$ , The LIGO Scientific Collaboration et al. 2020a) and GW190814 ( $q = 0.112^{+0.008}_{-0.009}$ , Abbott et al. 2020a) –, which are also atypical in stellar evolutionary models of isolated binaries (Gerosa et al. 2020b; Olejak et al. 2020; Zevin et al. 2020a). The object in the lower mass gap in GW190814 and a non-zero spin for the primary BH ( $a_1 = 0.43^{+0.16}_{-0.26}$ ) in GW190412 are consistent with a scenario in which the merging compact objects (COs) had experienced previous episode(s) of mergers or significant accretion. These events suggest that growth by gas accretion or hierarchical mergers may be common among COs (see e.g. O’Leary et al. 2016; Gerosa et al. 2020b; Abbott et al. 2020c; Hamers & Safarzadeh 2020; Rodriguez et al. 2020; Safarzadeh et al. 2020b; Safarzadeh & Haiman 2020; Yang et al. 2020b; Liu & Lai 2020; Tagawa et al. 2021a,b; Samsing et al. 2020).

Hierarchical mergers may occur in dynamical environ-

ments, such as globular clusters (GCs), nuclear star clusters (NSCs), and active galactic nucleus (AGN) accretion disks. In GCs, up to  $\sim 10 - 20\%$  of detected mergers may be caused by high-generation (high- $g$ ) BHs depending on spin magnitudes of 1g BHs (O’Leary et al. 2016; Rodriguez et al. 2019). Repeated mergers of BHs and stars may produce intermediate-mass BHs (IMBHs, BHs with masses of  $\sim 100 - 10^4 M_{\odot}$ ) in NSCs without supermassive BHs (SMBHs, Antonini et al. 2019; Askar et al. 2020; Mapelli et al. 2020). In NSCs with SMBHs, it is uncertain how often hierarchical mergers occur (e.g. Arca Sedda 2020).

In AGN disks, hierarchical mergers are predicted to be frequent due to the high escape velocity and efficient binary formation and evolution facilitated by gaseous (Yang et al. 2019; McKernan et al. 2020b) and stellar interactions (Tagawa et al. 2020b). Yang et al. (2019) and McKernan et al. (2020b,a) identified the expected mass ratio and spin distribution of hierarchical mergers in hypothetical migration traps (MTs) of AGN disks, defined to be regions where objects accumulate rapidly as they interact with the accretion disks analogously to planetary migration.<sup>1</sup> Tagawa et al. (2020a, 2021b) showed that hierarchical mergers take place in AGN disks without MTs and derived the corresponding mass and spin distributions self-consistently. In the latter models (e.g. Tagawa et al. 2020a), the mass and spin distributions of merging BHs are significantly different compared to those in the former models. This is mainly due to binary-single interactions which take place frequently at large orbital radii where the gas density is very low and gas effects drive the binaries toward merger more slowly and allow ample time for such binary-single interactions.

Several authors have investigated the properties of GWs associated with hierarchical mergers (Gerosa & Berti 2017; Yang et al. 2019; Kimball et al. 2020a; Doctor et al. 2020). Gerosa & Berti (2017) estimated the fraction of future detected sources contributed by hierarchical mergers under the assumption that first-generation (1g) BHs have a flat spin distribution and binary components are drawn independently. Fishbach et al. (2017) estimated the required number of events to detect hierarchical mergers using the distribution of the BH spin magnitudes. Doctor et al. (2020) constructed a toy model to obtain the properties of hierarchical mergers from the distribution of subpopulations for BHs under various assumptions for coagulation and depletion in the population and constrained parameters using LIGO/Virgo O1–O2 data. Kimball et al. (2020a) examined whether the observed events in the same catalog are compatible with hierarchical mergers particularly in GCs. These models found no evidence for a high rate of hierarchical mergers in this early catalog. More recently, by analyzing the ensemble of events detected during LIGO/Virgo’s O1–O3a observing runs, Kimball et al. (2020b) and Tiwari & Fairhurst (2020) found preference for at least one, but probably multiple hierarchical mergers in the detected sample. The conclusion of Kimball et al. (2020b) strongly

<sup>1</sup> Note that the orbital radii where this takes place were derived by assuming Type-I migration (Bellovary et al. 2016), but these assumptions may be inconsistent for BHs embedded in AGN disks as gaps may be opened in the accretion disks (see e.g. Eqs. 45–46 Kocsis et al. 2011). Also, Pan & Yang (2021) found that the traps can disappear if radiation pressure is correctly accounted for.

depends on the assumed escape velocity in the host environment, with higher escape velocities favoring a larger number of hierarchical mergers.

In this paper, we focus on distributions of the effective and precession spin parameters ( $\chi_{\text{eff}}$  and  $\chi_p$ ) and the chirp mass ( $m_{\text{chirp}}$ ), and predict characteristic features in them expected from hierarchical mergers. We use  $m_{\text{chirp}}$  as this variable is most precisely determined by GW observations, and  $\chi_{\text{eff}}$  and  $\chi_p$  as these characterize the BH spin magnitudes in a binary.

Here,  $\chi_{\text{eff}}$  and  $\chi_p$  are defined as

$$\chi_{\text{eff}} = \frac{m_1 a_1 \cos \theta_1 + m_2 a_2 \cos \theta_2}{m_1 + m_2} \quad (1)$$

and

$$\chi_p = \max \left( a_1 \sin \theta_1, q \frac{4q+3}{4+3q} a_2 \sin \theta_2 \right) \quad (2)$$

(Hamam et al. 2014; Schmidt et al. 2015), where  $m_1$  and  $m_2$  are the masses,  $a_1$  and  $a_2$  are the spin magnitudes,  $\theta_1$  and  $\theta_2$  are the angles between the orbital angular momentum directions and the BH spins of the binary components,  $q \equiv m_2/m_1 \leq 1$  is the mass ratio, and  $m_{\text{chirp}} \equiv (m_1 m_2)^{3/5} (m_1 + m_2)^{-1/5}$ . We find that intrinsic properties (maximum mass and typical spin magnitude) of 1g BHs can be constrained by recovering the features, which enables us to distinguish astrophysical models. By analyzing the GW data obtained in LIGO/Virgo O1–O3a, we reconstruct the intrinsic properties of the observed merging BH populations, and identify the astrophysical population models most consistent with the data. Finally, using mock GW data, we estimate how well parameters characterizing the spin distribution can be recovered in future catalogs depending on the number of events.

The paper is organized as follows. In § 2, we describe our method to construct mock GW data and detect signatures for hierarchical mergers. We present our main results in § 3, and give our conclusions in § 4.

## 2. METHOD

### 2.1. Overview

We perform the following analyses in this paper:

- (i) identify and characterize features expected in hierarchical mergers using mock GW data (§ 3.1),
- (ii) investigate whether such features are consistent with observed GW data (§ 3.2.1),
- (iii) assess how well model predictions match observed GW data (§ 3.2.2), and
- (iv) understand how well the features for hierarchical mergers can be reconstructed with varying the number of events using mock GW data (§ 3.3).

We adopt three different sets of mass and spin distributions:

- (A) actual GW data derived in LIGO/Virgo O1–O3a,
- (B) mock data produced by an  $N$ -body toy model (§ 2.2), and

(C) mock data produced by a physical model for mergers in AGN disks (adapted from our simulations in Tagawa et al. 2021b).

We introduce a simple model (B) because it allows us to explore hierarchical mergers more generically. In the analyses (i), (iii), and (iv), we use the model (B), while we also use the physically motivated model (C) in (iii) for comparison. Actual GW data (A) is used in (ii) and (iii). To identify features in the distributions representative of hierarchical mergers in (ii) and (iv), we use a simple analytic model characterizing the spin distribution profile (§ 2.3.1). In the analysis (iii), we use a Bayes factor to assess relative likelihoods of models.

In the analyses, we mostly use  $\chi_{\text{typ}} \equiv (\chi_{\text{eff}}^2 + \chi_p^2)^{1/2}$  as it characterizes the spin magnitudes of BHs in binaries. It is easily calculated from the quantities  $\chi_{\text{eff}}$  and  $\chi_p$  taken from Abbott et al. (2019a), Abbott et al. (2020b), and Gerosa et al. (2020a).

## 2.2. Constructing mock GW data

To understand and analyze the distributions of  $\chi_{\text{eff}}$ ,  $\chi_p$ , and  $m_{\text{chirp}}$  typically expected in hierarchical mergers, we employ mock GW data.

### 2.2.1. Overall procedure

We construct mock data by following the methodology of Doctor et al. (2020):

- 1 Sample  $N_{1g}$  BHs from 1g population as described in § 2.2.2. We set  $N_{1g} = 10^6$  to ensure a sufficient number for detectable mergers. We call this sample  $S$ .
- 2 Choose  $\omega N_{\text{ng}}$  pairs from  $S$  by weighing the pairing probability  $\Gamma$  (§ 2.2.2), where  $\omega$  is the fraction of BHs that merge at each step, and  $N_{\text{ng}}$  is the number of BHs in the sample  $S$  ( $N_{\text{ng}} = N_{1g}$  in the first iteration).
- 3 Compute the remnant mass and spin, and the kick velocity for merging pairs assuming random directions for BH spins, where we use the method described in Tagawa et al. (2020a). Update the sample  $S$  by removing BHs that have merged, and adding merged remnants if the kick velocity is smaller than the escape velocity ( $v_{\text{esc}}$ ).
- 4 Repeat steps 2-3 for  $N_s$  steps.
- 5 Determine the fraction of detectable mergers by assessing whether signal-to-noise ratio (SNR) of mergers exceeds the detection criteria (§ 2.2.3). Randomly choose  $N_{\text{obs}}$  observed mergers from the detectable merging pairs. Add observational errors following § 2.2.3, and construct a mock GW dataset.

By changing the underlying parameters of the merging binaries in mock GW data ( $\lambda_0$ ; presented in the next section), we can construct various  $\chi_{\text{eff}}$ ,  $\chi_p$  and  $m_{\text{chirp}}$  distributions expected in hierarchical mergers. For example,  $N_s$  and  $\omega$  influences the fraction of hierarchical mergers ( $\propto \sim \omega^{N_s}$ ), while  $N_s$  specifies the maximum generation and mass of BHs.

### 2.2.2. First generation BHs and pairing

We assume that the masses of 1g BHs are drawn from the power-law distribution as

$$p_{m_{1g}} \propto \begin{cases} m_{1g}^{-\alpha} & \text{for } m_{\min} < m_{1g} < m_{\max}, \\ 0 & \text{otherwise,} \end{cases} \quad (3)$$

where  $\alpha$  is the power-law slope,  $m_{\min}$  and  $m_{\max}$  are the minimum and maximum masses.

We set the dimensionless spin magnitude for 1g BHs to

$$a_{\text{ini}} = |a_{\text{ave}} + a_{\text{uni}} U[-1 : 1]| \quad (4)$$

where  $U[-1 : 1]$  represent uniform distribution randomly chosen from -1 to 1, and  $a_{\text{ave}}$  and  $a_{\text{uni}}$  are parameters characterising initial spins of 1g BHs. We assume that the spin magnitude for 1g BHs does not depend on the masses of 1g BHs. This assumption may be justified for single BHs, for which slow rotation is motivated by theoretical considerations (Fuller & Ma 2019). Here we assume  $a_{\text{ave}} = a_{\text{uni}} = 0$  in the fiducial model. On the other hand, for mergers of field binaries (FBs), a large fraction of BHs may experience tidal synchronization, and the dispersion of the BH spin magnitudes decreases with BH masses (e.g. Hotokezaka & Piran 2017; Bavera et al. 2019; Safarzadeh et al. 2020a). The spin distribution expected in this pathway is considered in § 3.1.2.

We assume the redshift distribution of merging BHs as

$$p_z \propto \frac{dV_c}{dz} \frac{1}{1+z} \quad (5)$$

so that a merger rate density is uniform in comoving volume and source-frame time. Here,  $dV_c/dz$  is calculated assuming  $\Lambda$ CDM cosmology with the Hubble constant  $H_0 \simeq 70$  km/s/Mpc, the matter density today  $\Omega_{\text{m}0} = 0.24$ , and the cosmological constant today  $\Omega_{\Lambda 0} = 0.76$  (Planck Collaboration et al. 2016). We also investigate different choices in § 3.1.1 (see also Fishbach et al. 2018; Yang et al. 2020a). We set the maximum redshift to be 1.5 considering LIGO/Virgo sensitivities (The LIGO Scientific Collaboration et al. 2019).

To draw merging pairs, we simply assume that the interaction rate depends on the binary masses with a form

$$\Gamma \propto (m_1 + m_2)^{\gamma_t} q^{\gamma_q} \quad (6)$$

as employed in Doctor et al. (2020). This parameterization enables us to mimic the effects that massive and equal-mass binaries are easy to merge in plausible models due to exchanges at binary-single interactions, mass segregation in clusters, interaction with ambient gas, mass transfer, or common-envelope evolution (e.g. O’Leary et al. 2016; Rodriguez et al. 2019; Tagawa et al. 2021b; Olejak et al. 2020).

Using the model described above and adding observational errors (§ 2.2.3), we can construct a mock observational dataset. The parameter set characterizing a mock dataset is  $\lambda_0 = \{\alpha, m_{\min}, m_{\max}, a_{\text{ave}}, a_{\text{uni}}, \gamma_t, \gamma_q, \omega, N_s, v_{\text{esc}}, N_{\text{obs}}\}$ . The fiducial choice of  $\lambda_0$  is described in § 2.2.4 and Table 1.

### 2.2.3. Mock observational errors

To construct mock GW data, we need to put observational errors on observables. The true values of observables  $\boldsymbol{\theta}$  are produced through the procedures in § 2.2.1 and § 2.2.2 assuming a set of the population parameters  $\boldsymbol{\lambda}_0$ . To incorporate observational errors to the mock data, we refer to the prescription in Fishbach & Holz (2020). We assume that the binary is detected if the SNR of the signal in a single detector exceeds 8. We set the typical SNR,  $\rho_0$ , of a binary with parameters  $m_{\text{chirp}}$ ,  $\chi_{\text{eff}}$ , and the luminosity distance  $d_L$  to

$$\rho_0 = 8 \left[ \frac{m_{\text{chirp}}(1+z)}{m_{\text{chirp},8}} \right]^{5/6} \frac{d_{\text{L},8}}{d_L} \left( 1 + \frac{3}{8} \chi_{\text{eff}} \right) \quad (7)$$

where we fix  $m_{\text{chirp},8} = 10 \text{ M}_\odot$  and  $d_{\text{L},8} = 1 \text{ Gpc}$  (see eq. 26 in Fishbach et al. 2018). This scaling approximates the amplitude of a GW signal,  $m_{\text{chirp},8}$  and  $d_{\text{L},8}$  are chosen to roughly match the typical values detected by LIGO at design sensitivity (Chen et al. 2017), and the dependence on  $\chi_{\text{eff}}$  roughly reproduces results in The LIGO Scientific Collaboration et al. (2019). We calculate  $d_L$  from  $z$  assuming  $\Lambda\text{CDM}$  cosmology as stated above. The true SNR depends on the angular factor  $\Theta$ , and is given by

$$\rho = \rho_0 \Theta. \quad (8)$$

$\Theta$  plays the combined role of the sky location, inclination, and polarization on the measured GW amplitude. We tune the width of the distribution to control the uncertainty of the measured signal strength, which in turn controls the uncertainty on the measured luminosity distance. We simply set  $\Theta$  to a log-normal distribution with

$$\log \Theta \sim N \left( 0, \frac{0.3}{1 + \frac{\rho_0}{8}} \right) \quad (9)$$

following Fishbach et al. (2018).

From the true parameters  $\rho$ ,  $m_{\text{chirp}}(1+z)$ ,  $z$ ,  $\chi_{\text{eff}}$  and  $\Theta$ , we assume that the four parameters, the SNR ( $\rho_{\text{obs}}$ ), the chirp mass ( $m_{\text{chirp},\text{obs}}$ ),  $\chi_{\text{eff},\text{obs}}$ , and  $\chi_{\text{p},\text{obs}}$ , are given with errors as below. We assume that the fractional uncertainty on the detector-frame chirp mass is

$$\sigma_{m_{\text{chirp}}} = \frac{8}{\rho_{\text{obs}}} 0.04 m_{\text{chirp}}(1+z), \quad (10)$$

that on the SNR is

$$\sigma_\rho = 1 \quad (11)$$

following Fishbach & Holz (2020), and that on  $\chi_{\text{eff}}$  and  $\chi_{\text{p}}$  is, respectively,

$$\sigma_{\chi_{\text{eff}}} = 0.1 \frac{8}{\rho_0}, \quad (12)$$

and

$$\sigma_{\chi_{\text{p}}} = 0.2 \frac{8}{\rho_0}, \quad (13)$$

which roughly match typical observational error magnitudes in Abbott et al. (2019b) and Gerosa et al. (2020a). We assume that the observed median values  $\tilde{m}_{\text{chirp},\text{obs}}$ ,  $\tilde{\rho}_{\text{obs}}$ ,  $\tilde{\chi}_{\text{eff},\text{obs}}$ , and  $\tilde{\chi}_{\text{p},\text{obs}}$ , respectively, from a normal distribution centered on the true values  $m_{\text{chirp}}(1+z)$ ,  $\rho$ ,  $\chi_{\text{eff}}$ , and  $\chi_{\text{p}}$  with the standard deviation  $\sigma_{m_{\text{chirp}}}$ ,  $\sigma_\rho$ ,  $\sigma_{\chi_{\text{eff}}}$ , and

$\sigma_{\chi_{\text{p}}}$ . We further assume that the posterior distributions of  $m_{\text{chirp}}$ ,  $\rho$ ,  $\chi_{\text{eff}}$ , and  $\chi_{\text{p}}$  including errors for GW data in the  $i^{\text{th}}$  event are, respectively, calculated by drawing from a normal distribution centered on  $\tilde{m}_{\text{chirp},\text{obs}}$ ,  $\tilde{\rho}_{\text{obs}}$ ,  $\tilde{\chi}_{\text{eff},\text{obs}}$ , and  $\tilde{\chi}_{\text{p},\text{obs}}$  with the standard deviation  $\sigma_{m_{\text{chirp}}}$ ,  $\sigma_\rho$ ,  $\sigma_{\chi_{\text{eff}}}$ , and  $\sigma_{\chi_{\text{p}}}$ . An observed value of  $z$  is calculated from  $d_L$  derived by incorporating the observed values to Eq. (7) and the relation between  $z$  and  $d_L$  so that Eq. (7) is valid for derived  $z$ .

#### 2.2.4. Numerical choices

Table 1 lists the parameter values adopted in the fiducial model. Referring to Fuller & Ma (2019), we set small BH spin magnitudes for 1g BHs as  $a_{\text{ave}} = a_{\text{uni}} = 0$ . The power-law slope in the mass function for 1g BHs is given as  $\alpha = 1$ . Assuming mergers in (active phase of) NSCs, where hierarchical mergers are probably most frequent, we set  $m_{\text{max}} = 20 \text{ M}_\odot$  as NSCs are mainly metal rich (e.g. Do et al. 2018; Schödel et al. 2020),  $v_{\text{esc}} = 1000 \text{ km/s}$  typically expected for merging sites of binaries (Tagawa et al. 2020b),  $\gamma_t = 2$  and  $\gamma_q = 2$  as high- and equal-mass BHs are easier to merge in dynamical environments, and  $\omega = 0.1$  and  $N_s = 4$  to reproduce frequent hierarchical mergers (Table 2, Tagawa et al. 2021b).

### 2.3. Reconstruction of the spin distribution

Here, we present a way to detect features for hierarchical mergers that possibly appear in the distribution of spins and masses.

#### 2.3.1. Model characterizing the spin distribution

As universal trends for hierarchical mergers are presented in spin and mass distributions of merging binaries (§ 3.1.1), we investigate how well such trends can be reconstructed using a finite number of events. To do this, we replace the procedure above with a simple parametric analytic toy model, directly describing the distribution of the three variables ( $\boldsymbol{\theta} = \{\chi_{\text{eff}}, \chi_{\text{p}}, m_{\text{chirp}}\}$ ) in terms of a set of the parameters ( $\boldsymbol{\lambda}$ ) as

$$p(\boldsymbol{\theta}|\boldsymbol{\lambda}) = N(\chi_{\text{typ}}|\mu_\chi, \sigma_\chi) T[-1, 1], \quad (14)$$

where  $N(x_0|x_1, x_2)$  represents the probability to return  $x_0$  for the normal distribution with the mean  $x_1$  and the standard deviation  $x_2$ ,  $T[-1, 1]$  means to truncate the normal distribution to the range  $[-1, 1]$  and normalize  $N$  so that the integral of  $N$  in this range is 1,  $\chi_{\text{typ}} \equiv (\chi_{\text{p}}^2 + \chi_{\text{eff}}^2)^{1/2}$ ,

$$\mu_\chi = \begin{cases} a_\mu m_{\text{chirp}} + b_\mu & \text{for } m_{\text{chirp}} < m_{\text{crit},\mu} \\ b_\mu & \text{for } m_{\text{chirp}} \geq m_{\text{crit},\mu} \end{cases}, \quad (15)$$

and

$$\sigma_\chi = \begin{cases} a_\sigma m_{\text{chirp}} + b_\sigma & \text{for } m_{\text{chirp}} < m_{\text{crit},\sigma} \\ b_\sigma & \text{for } m_{\text{chirp}} \geq m_{\text{crit},\sigma} \end{cases}. \quad (16)$$

We use  $\chi_{\text{typ}}$  since it roughly represents the spin magnitudes of BHs in a binary.

Hence, this model has six parameters  $\boldsymbol{\lambda} = \{a_\mu, b_\mu, m_{\text{crit},\mu}, a_\sigma, b_\sigma, m_{\text{crit},\sigma}\}$  characterizing the  $\chi_{\text{typ}}$  profile as a function of  $m_{\text{chirp}}$ . The functional form of the model (eq. 14) is motivated by the prediction that hierarchical mergers favor a plateau in the distribution

of  $\bar{\chi}_{\text{typ}}$  vs.  $m_{\text{chirp}}$  at high  $m_{\text{chirp}}$  as the BH spin magnitudes roughly converge to a constant value of  $\sim 0.7$  after mergers, while  $\bar{\chi}_{\text{typ}}$  almost linearly approaches the value at the plateau from lower  $m_{\text{chirp}}$  (see Fig. 1).

The model parameters,  $\boldsymbol{\lambda}$ , are estimated from GW data through a Bayesian analysis, whose details are described in the next section.

### 2.3.2. Bayesian analysis

To derive the posterior distribution of  $\boldsymbol{\lambda}$  from a dataset  $\{\mathbf{d}_i\}$ ,  $p(\boldsymbol{\lambda}|\{\mathbf{d}_i\})$ , we use the Bayesian formalism as follows. Here,  $\mathbf{d}_i$  encodes the measurable parameters ( $\boldsymbol{\theta}$ ) and also includes their random noise in the  $i^{\text{th}}$  event. Bayes' rule gives

$$p(\boldsymbol{\lambda}|\{\mathbf{d}_i\}) = \frac{p(\{\mathbf{d}_i\}|\boldsymbol{\lambda})\pi(\boldsymbol{\lambda})}{p(\{\mathbf{d}_i\})}, \quad (17)$$

where  $p(\{\mathbf{d}_i\}|\boldsymbol{\lambda})$  is the likelihood to obtain  $\{\mathbf{d}_i\}$  for  $\boldsymbol{\lambda}$ ,  $\pi(\boldsymbol{\lambda})$  is the prior probability for the model parameters  $\boldsymbol{\lambda}$ , and the evidence  $p(\{\mathbf{d}_i\})$  is the integral of the numerator over all  $\boldsymbol{\lambda}$ .

We assume that each GW detection is independent, so that

$$p(\{\mathbf{d}_i\}|\boldsymbol{\lambda}) = \prod_{i=1}^{N_{\text{obs}}} p(\mathbf{d}_i|\boldsymbol{\lambda}). \quad (18)$$

The probability of making observation  $i$  is

$$p(\mathbf{d}_i|\boldsymbol{\lambda}) = \frac{\int d\boldsymbol{\theta} p(\mathbf{d}_i|\boldsymbol{\theta})p(\boldsymbol{\theta}|\boldsymbol{\lambda})}{A(\boldsymbol{\lambda})}, \quad (19)$$

where the normalization factor  $A(\boldsymbol{\lambda})$  is given by

$$\begin{aligned} A(\boldsymbol{\lambda}) &= \int_{\mathbf{d} > \text{threshold}} d\mathbf{d} \int d\boldsymbol{\theta} p(\mathbf{d}|\boldsymbol{\theta})p(\boldsymbol{\theta}|\boldsymbol{\lambda}) \\ &= \int d\boldsymbol{\theta} p_{\text{det}}(\boldsymbol{\theta})p(\boldsymbol{\theta}|\boldsymbol{\lambda}), \end{aligned} \quad (20)$$

$$p_{\text{det}}(\boldsymbol{\theta}) = \int_{\mathbf{d} > \text{threshold}} p(\mathbf{d}|\boldsymbol{\theta})d\mathbf{d} \quad (21)$$

is the detection probability for a given set of parameters, and ‘‘threshold’’ denotes that the event  $\mathbf{d}$  is detectable when  $\mathbf{d}$  is above the threshold. To reduce computational costs, we assume that  $A(\boldsymbol{\lambda})$  is constant. This assumption does not affect our results as  $A(\boldsymbol{\lambda})$  varies by less than a factor of 1.1 if the spin directions of BHs are assumed to be isotropic, meaning that the variation of  $A(\boldsymbol{\lambda})$  per each steps in the Monte Carlo method (§ 2.3.3) is negligible. This is because the detection probability is influenced only by  $\chi_{\text{eff}}$  by changing  $\boldsymbol{\lambda}$  (see Eqs. 7 and 14), and the reduction and enhancement of the detectable volume for mergers with negative and positive  $\chi_{\text{eff}}$  are mostly cancelled out.

The likelihood  $p(\mathbf{d}_i|\boldsymbol{\theta})$  can be rewritten in terms of the posterior probability density function (PDF)  $p(\boldsymbol{\theta}|\mathbf{d}_i)$  that is estimated in the analysis assuming prior  $\pi(\boldsymbol{\theta})$  as

$$p(\mathbf{d}_i|\boldsymbol{\theta}) = \frac{p(\boldsymbol{\theta}|\mathbf{d}_i)p(\mathbf{d}_i)}{\pi(\boldsymbol{\theta})}. \quad (22)$$

The posterior PDF  $p(\boldsymbol{\theta}|\mathbf{d}_i)$  has information on errors, and it is often discretely sampled with  $S_i$  samples from the posterior,  $\{^j\boldsymbol{\theta}^{(i)}\}$ , for  $j \in [1, S_i]$ . Because the samples are drawn according to the posterior, the parameter space volume associated with each sample is inversely proportional to the local PDF,  $d^j\boldsymbol{\theta}^{(i)} \propto [p(^j\boldsymbol{\theta}^{(i)}|\mathbf{d}^{(i)})]^{-1}$ , which allows us to replace the integral with a discrete sum (e.g. Mandel et al. 2019; Vitale et al. 2020). Overall, the posterior distribution of  $\boldsymbol{\lambda}$  is given as

$$\begin{aligned} p(\boldsymbol{\lambda}|\{\mathbf{d}_i\}) &= \frac{\pi(\boldsymbol{\lambda})}{p(\{\mathbf{d}_i\})} \prod_{i=1}^{N_{\text{obs}}} \frac{\frac{1}{S_i} \sum_{j=1}^{S_i} p(^j\boldsymbol{\theta}^{(i)}|\boldsymbol{\lambda}) \frac{p(\mathbf{d}_i)}{\pi(\boldsymbol{\theta})}}{A(\boldsymbol{\lambda})} \\ &\propto \pi(\boldsymbol{\lambda}) \prod_{i=1}^{N_{\text{obs}}} \frac{\frac{1}{S_i} \sum_{j=1}^{S_i} p(^j\boldsymbol{\theta}^{(i)}|\boldsymbol{\lambda}) \frac{1}{\pi(\boldsymbol{\theta})}}{A(\boldsymbol{\lambda})}, \end{aligned} \quad (23)$$

where we factor out the evidence factors  $p(\{\mathbf{d}_i\})$  and  $\prod_{i=1}^{N_{\text{obs}}} p(\mathbf{d}_i)$  since it is independent of  $\boldsymbol{\lambda}$  and does not affect the relative values of the posterior  $p(\boldsymbol{\lambda}|\{\mathbf{d}_i\})$ . We use a flat prior distribution for  $\pi(\boldsymbol{\lambda})$ , while we set  $\pi(\boldsymbol{\theta}) \propto d_L^2(z)$  following the standard priors used in the LIGO/Virgo analysis of individual events (Veitch et al. 2015). We set  $S_i = 3N_{\text{obs}}$  so that we can take into account uncertainties whose probability is in the order of  $\sim 1/N_{\text{obs}}$ .

### 2.3.3. Markov chain Monte Carlo methods

We calculate the posterior distribution (Eq. 23) using Markov chain Monte Carlo (MCMC) methods. We track one chain for  $10^7$  steps, set the first half to a burn-in period, check convergence by verifying that values for parameters after the burn-in period are oscillating around a constant average and dispersion. We adopt Metropolis-Hastings algorithm (e.g. Hastings 1970), and set a proposal distribution to the normal distribution with the values at each step as the means and the standard deviations for  $a_\mu$ ,  $b_\mu$ ,  $m_{\text{crit},\mu}$ ,  $a_\sigma$ ,  $b_\sigma$  and  $m_{\text{crit},\sigma}$  to be 0.0005  $M_\odot^{-1}$ , 0.004, 0.1  $M_\odot$ , 0.001  $M_\odot^{-1}$ , 0.002, and 0.1  $M_\odot$ , respectively. The standard deviations of the proposal distribution are roughly given by the typical standard deviations of the posterior distribution divided by  $\sim 4$  as this setting works well for convergence. We do not pose thinning to a posterior distribution as the autocorrelation for each variable between adjacent steps is already as small as  $\lesssim 10^{-5}$ . We restrict  $m_{\text{crit},\mu}$  and  $m_{\text{crit},\sigma}$  in the ranges from  $m_{\text{min}}$  to the maximum  $m_{\text{chirp}}$  among observed events.

## 3. RESULTS

In § 3.1, we investigate characteristic features in hierarchical mergers, using our flexible tool (§ 2.2) to generate mock GW datasets for a large range of input parameter combinations. In § 3.2, we analyze GW data observed in LIGO/Virgo O1–O3a. We first derive signatures and properties of hierarchical mergers (§ 3.2.1), using the simple fitting formula for spin vs. chirp mass (§ 2.3.1). We then assess (§ 3.2.2) how well the predictions in our mock GW catalogs and in our physical AGN disk models (Tagawa et al. 2021b) in fact match these observed GW data. Finally, in § 3.3, we analyze mock GW

**Table 1**  
Fiducial values of our model parameters.

Parameter	Fiducial value
The number of observed events	$N_{\text{obs}} = 1000$
Frequency of mergers for high-mass binaries	$\gamma_t = 2$
Frequency of mergers for equal-mass binaries	$\gamma_q = 2$
The spin magnitudes for 1g BHs	$a_{\text{ave}} = 0, a_{\text{uni}} = 0$
Maximum and minimum masses for 1g BHs	$m_{\text{max}} = 20 M_{\odot}, m_{\text{min}} = 5 M_{\odot}$
Power-law exponent in the mass function for 1g BHs	$\alpha = 1$
Fraction of BHs that merges at each step	$\omega = 0.1$
Number of merger steps	$N_s = 4$
Escape velocity of systems hosting BHs	$v_{\text{esc}} = 1000 \text{ km/s}$
The parameter for correlation between the steps and the redshift	$w_z = \infty$ (no correlation)

**Table 2**

Properties of hierarchical mergers in our models. The first and second columns indicate the model number and its variation from the fiducial model (Table 1). The third and fourth columns show the fraction of high-g mergers among all and detectable mergers, respectively. The fifth column shows the maximum chirp mass among  $N_{\text{obs}} = 10^3$  detectable mergers (except for different  $N_{\text{obs}}$  in models M2, M3, M21–M24 as noted). The sixth and seventh columns show the average and the standard deviation of  $\bar{\chi}_p$  among all merging pairs.

model	Parameter	high-g fraction	high-g detection fraction	$m_{\text{chirp}} [M_{\odot}]$	$\bar{\chi}_p$	$\sigma(\chi_p)$
M1	Fiducial	0.33	0.68	56	0.17	0.26
M2	$N_{\text{obs}} = 50$	0.33	0.78	38	0.17	0.26
M3	$N_{\text{obs}} = 10^4$	0.33	0.77	60	0.17	0.26
M4	$N_s = 1$	0	0	15	0	0
M5	$N_s = 2$	0.15	0.40	23	0.077	0.19
M6	$N_s = 3$	0.25	0.61	42	0.13	0.24
M7	$N_s = 5$	0.38	0.80	72	0.20	0.27
M8	$a_{\text{uni}} = 1$	0.32	0.73	52	0.50	0.21
M9	$a_{\text{ave}} = 0.99$	0.31	0.70	51	0.75	0.20
M10	$a_{\text{ave}} = 0.66, a_{\text{uni}} = 0.1$	0.33	0.72	55	0.55	0.13
M11	$\gamma_t = 0$	0.22	0.50	31	0.11	0.22
M12	$\gamma_q = 0$	0.39	0.71	36	0.19	0.25
M13	$\omega = 0.01$	0.043	0.089	23	0.022	0.11
M14	$\omega = 0.03$	0.13	0.37	33	0.066	0.18
M15	$v_{\text{esc}} = 30 \text{ km/s}$	0.29	0.61	31	0.15	0.25
M16	$\alpha = 2$	0.32	0.75	52	0.16	0.25
M17	$m_{\text{max}} = 30 M_{\odot}$	0.35	0.73	70	0.18	0.26
M18	$w_z = 2$	0.33	0.73	46	0.17	0.26
M19	$w_z = 0.05$	0.33	0.79	59	0.17	0.26
M20	$N_s = 2, \omega = 0.001$	0.0014	0.0040	17	0.001	0.02
M21	$N_{\text{obs}} = 50, N_s = 3$	0.25	0.62	28	0.13	0.24
M22	$N_{\text{obs}} = 50, N_s = 2$	0.15	0.28	24	0.077	0.19
M23	$N_{\text{obs}} = 50, N_s = 2, \omega = 0.05$	0.077	0.18	19	0.040	0.14
M24	$N_{\text{obs}} = 50, N_s = 2, \omega = 0.03$	0.046	0.14	19	0.023	0.11
M25	Globular cluster (GC)	0.063	0.17	44	0.030	0.13
M26	Field binary (FB)	0	0	23	0	0
M27	Migration trap (MT)	0.31	0.80	42	0	0

data, and investigate how well the signatures of hierarchical models, described by the simple fitting formulae ( $\bar{\chi}_{\text{typ}}$  vs.  $m_{\text{chirp}}$ ), can be recovered from future, larger GW catalogs.

### 3.1. Profiles for average spin parameters

#### 3.1.1. Dependence on population parameters

We first show the parameter dependence of the  $\bar{\chi}_{\text{typ}}$  profile as a function of  $m_{\text{chirp}}$  using mock GW events, in which hierarchical mergers are assumed to be frequent. In Table 2, we list the model varieties we have investigated. These include the fiducial model (M1), and 26 different varieties (models M2–M27). We exam-

ine different choices of the number of detected mergers (models M2 and M3), the steps to create samples for hierarchical mergers (models M4–M7), the initial spin magnitudes of 1g BHs (models M8–M10), and the mass function (models M16, M17), pairing probability (models M11 and M12), the fraction of mergers in each step (models M13 and M14), the escape velocity of the system (model M15), the correlation between the steps and the redshift (models M18 and M19), and the fraction of hierarchical mergers (models M20–M24). We also investigate the several parameter sets mimicking different populations (models M25–M27, Table 3).

Fig. 1 shows the profiles for models M1–M27 (Table 2).

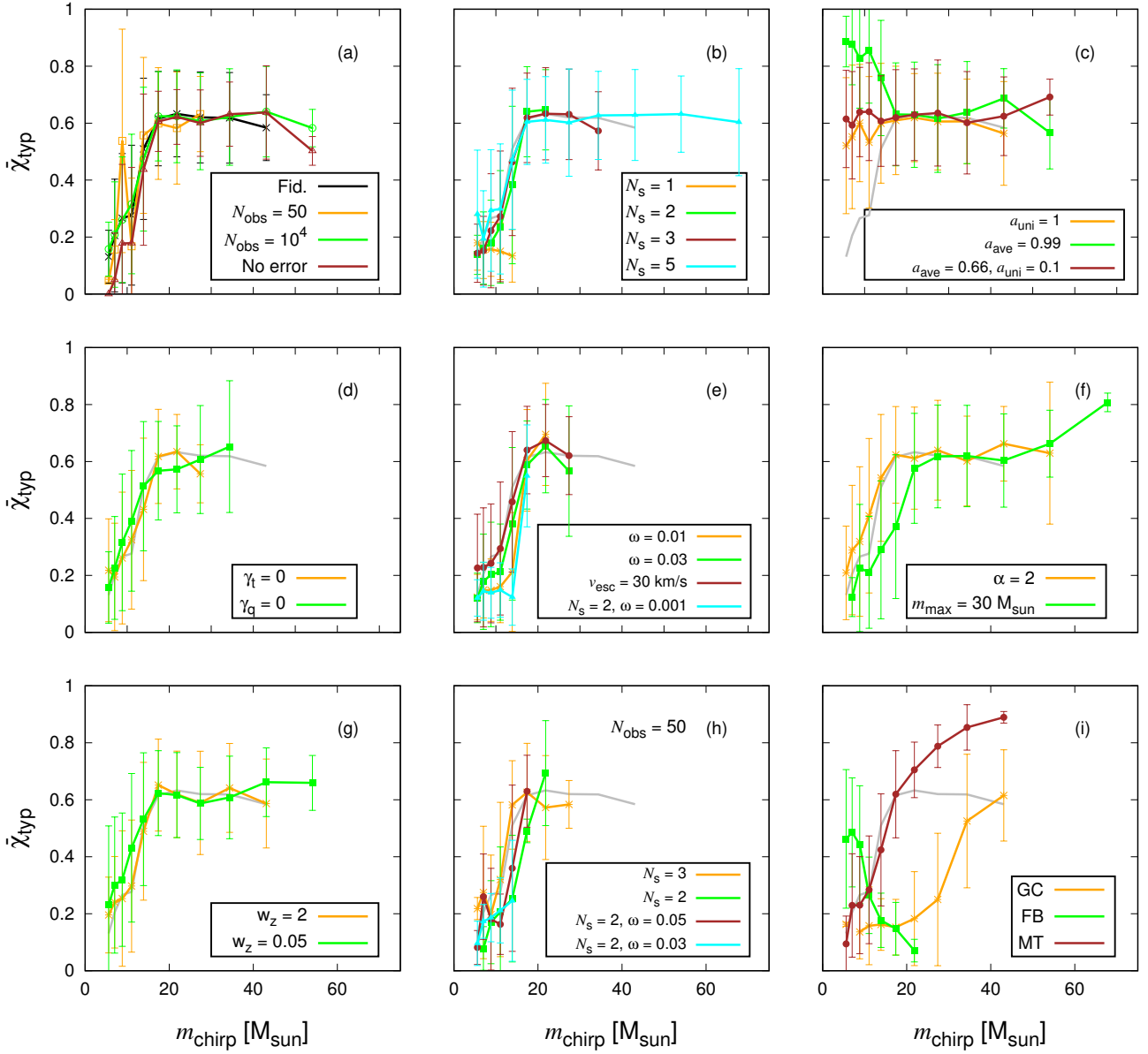


**Figure 1.** The mean dimensionless total spin  $\bar{\chi}_{\text{typ}}$  as a function of  $m_{\text{chirp}}$  for models M1–M27 (Table 2). We use  $N_{\text{obs}} = 10^3$  detectable mergers for models M1, M4–M20, M25–M27 while  $N_{\text{obs}} = 50$  and  $10^4$  for models M2, M21–M24 and M3, respectively. In panels (b)–(i), the profiles for model M1 are presented by gray lines. Bars correspond to  $1\sigma$  credible intervals.

We can see universal trends in the  $\bar{\chi}_{\text{typ}}$  profiles: (i) increase (or decrease) of  $\bar{\chi}_{\text{typ}}$  to  $\sim 0.6$  at low  $m_{\text{chirp}}$ . (ii) plateau of  $\bar{\chi}_{\text{typ}}$  with  $\sim 0.6$  at high  $m_{\text{chirp}}$ . Thus, the profile is roughly characterized by two lines if hierarchical mergers are frequent, mergers originate mostly from one population, and the typical spin magnitude for 1g BHs does not depend on their masses. The profile of  $\bar{\chi}_{\text{typ}}$  strongly depends on  $a_{\text{ave}}$ ,  $a_{\text{uni}}$ , and  $m_{\text{max}}$  (panels c and f), while it is less affected by the other parameters.

The typical value of  $\bar{\chi}_{\text{typ}} \sim 0.6$  at the plateau can be understood as follows. When masses and spin magnitudes between the primary and secondary BHs are similar ( $m_1 \sim m_2$  and  $a_1 \sim a_2 \sim a_0$ ) and the directions of

BH spins are isotropic, the typical magnitude of mass-weighted BH spins is

$$|\mathbf{a}_w| = \left\langle \left| \frac{m_1 \mathbf{a}_1 + m_2 \mathbf{a}_2}{m_1 + m_2} \right| \right\rangle \sim \frac{\sqrt{7}}{3} a_0, \quad (24)$$

where  $\langle \dots \rangle$  represents an average over the number of samples. If we approximate

$$\begin{aligned} \bar{\chi}_p &\simeq \langle |\mathbf{a}_0| |\cos\theta| \rangle \sim \frac{\pi}{4} a_0, \\ |\chi_{\text{eff}}| &\simeq \langle |\mathbf{a}_w| |\sin\theta| \rangle \sim \frac{1}{2} |\mathbf{a}_w|, \end{aligned} \quad (25)$$

then

$$\bar{\chi}_{\text{typ}} = \left( \overline{|\chi_{\text{eff}}|^2} + \bar{\chi}_{\text{p}}^2 \right)^{1/2} \sim \left[ \left( \frac{\sqrt{7}}{3} \frac{1}{2} \right)^2 + \left( \frac{\pi}{4} \right)^2 \right]^{1/2} a_0 \sim 0.90 a_0. \quad (26)$$

Since merged remnants typically have spin magnitudes of  $a_0 \sim 0.7$  (Buonanno et al. 2008),  $\bar{\chi}_{\text{typ}} \sim 0.6$  for mergers among high-g BHs, which is roughly consistent with the value at the plateau (Fig. 1). Note that when  $q \ll 1$ ,  $|\mathbf{a}_w| \sim a_0$  and so the average value is slightly enhanced to  $\bar{\chi}_{\text{typ}} \sim 0.93 a_0$ .

As  $m_{\text{max}}$  increases, the bending point between the two lines increases (gray and green lines in panel f). This is because  $m_{\text{max}}$  determines the critical mass above which all merging BHs are of high generations with high spins of  $\sim 0.7$ . As the bending point is not influenced by the other parameters, the maximum mass of 1g BHs can be estimated from the bending point of the  $\bar{\chi}_{\text{typ}}$  profile. Note that since the bending points of the  $\chi_{\text{p}}$  and  $\chi_{\text{eff}}$  profiles are similar in shape to that of the  $\bar{\chi}_{\text{typ}}$  profile for mergers with isotropic BH spins (panels a and b of Fig. 3), either  $\chi_{\text{typ}}$ ,  $\chi_{\text{p}}$  or  $\chi_{\text{eff}}$  can constrain the maximum mass of 1g BHs if the profiles are reconstructed well.

Additionally,  $a_{\text{ave}}$  and  $a_{\text{uni}}$  influence  $\bar{\chi}_{\text{typ}}$  at the smallest values of  $m_{\text{chirp}}$  (panel c). This suggests that typical spin magnitudes of 1g BHs can be presumed by spins at small  $m_{\text{chirp}}$ . However, note that  $\bar{\chi}_{\text{typ}}$  at small  $m_{\text{chirp}}$  is also influenced by the observational errors on  $\chi_{\text{p}}$  and  $\chi_{\text{eff}}$  (orange line in panel a). Due to the smaller errors on  $|\chi_{\text{eff}}|$  compared to  $\chi_{\text{p}}$ ,  $|\chi_{\text{eff}}|$  may constrain the typical spin values of 1g BHs more precisely using a number of events (green and orange lines in Fig. 3 a). Note that  $\bar{\chi}_{\text{p}} > |\chi_{\text{eff}}|$  when the BH spins are isotropic due to their definition.

With smaller number of iteration steps ( $N_s$ ), the maximum  $m_{\text{chirp}}$  becomes smaller because the generations of BHs are limited by  $N_s$  (panel b). Similarly, the maximum  $m_{\text{chirp}}$  decreases as  $N_{\text{obs}}$ ,  $\gamma_t$ ,  $\omega$ , or  $v_{\text{esc}}$  decreases or  $m_{\text{max}}$  increases (panels a, d, e, and f, Table 2). In these ways, the maximum  $m_{\text{chirp}}$  is influenced by a number of parameters, implying that the maximum  $m_{\text{chirp}}$  alone cannot constrain each of those parameters.

In panel (h), we can see how the features for hierarchical mergers in the  $\chi_{\text{typ}}$  profile are influenced by the fraction of hierarchical mergers for  $N_{\text{obs}} = 50$ . The plateau at high  $m_{\text{chirp}}$  is seen for  $N_s = 3$  (orange), while the rise of  $\chi_{\text{typ}}$  to  $\sim 0.6$  at low  $m_{\text{chirp}}$  is seen for  $N_s = 2$  with  $\omega \geq 0.05$  (green and brown). These suggest that with  $N_{\text{obs}} = 50$  the plateau and the rise of  $\chi_{\text{typ}}$  to  $\sim 0.6$  can be confirmed when the detection fraction of mergers of high-g BHs roughly exceeds  $\sim 0.5$  and  $\sim 0.15$ , respectively (models M21, M23, Table 2).

Here, we investigate the effect that mergers at larger iteration steps tend to occur at lower redshift because finite time needs to elapse between each generation and high-g mergers thus would take place after a significant delay compared to low-g mergers. To take this delay into account, we modify the redshift distribution of merging

**Table 3**

Adopted parameter values for several populations. The differences with respect to the fiducial model (Table 1) are listed.

Globular cluster (GC)	
1	$m_{\text{max}} = 45 M_{\odot}$
2	$N_s = 2$
3	$\omega = 0.03$
4	$v_{\text{esc}} = 30 \text{ km/s}$
Field binary (FB)	
1	$m_{\text{max}} = 30 M_{\odot}$
2	$N_s = 1$
3	$\theta_1 = \theta_2 = 0$
4	$a_{\text{uni}}$ follows Eq. (28)
Migration trap (MT)	
1	$\theta_1 = \theta_2 = 0$

BHs as

$$p_z \propto \frac{dV_c}{dz} \frac{1}{1+z} \exp \left( \frac{(t_L(z) - \mu_t)^2}{2\sigma_t^2} \right), \quad (27)$$

where  $t_L(z)$  is the look-back time, we set the average to  $\mu_t = t_{\text{typ}} \left( \frac{N_s - N_i + 1}{N_s} \right)$  and the standard deviation to  $\sigma_t = t_{\text{typ}} w_t$ ,  $N_i$  is the number of steps that the  $i^{\text{th}}$  merger is created,  $t_{\text{typ}}$  is the typical look-back time that mergers began to occur, which is set to 10 Gyr, and  $w_z$  is the parameter determining the strength of correlation between  $N_i$  and the time that mergers occur. A lower value of  $w_z$  makes mergers with high  $N_i$  occur at a lower  $z$ , and the fiducial model (Eq. 5) corresponds to  $w_z = \infty$ . The dependence of the  $\bar{\chi}_{\text{typ}}$  profile on  $w_z$  is shown in panel (g), suggesting that the correlation between the redshift and the generations of BHs has a negligible impact on the profile.

To summarize, the profile of  $\bar{\chi}_{\text{typ}}$  is mostly affected only by  $a_{\text{ave}}$ ,  $a_{\text{uni}}$ , and  $m_{\text{max}}$ , while the other parameters may affect the maximum  $m_{\text{chirp}}$  or the frequency of high-g mergers (Table 2).

### 3.1.2. Contribution from multiple populations

In the fiducial model (M1), the parameter values (Table 1) are roughly adjusted to reproduce properties of mergers in AGN disks outside of MTs (Tagawa et al. 2021b) or NSCs. The  $\chi_{\text{typ}}$  profile is similar but the  $m_{\text{chirp}}$  distribution is different between the fiducial model and physically motivated models derived in Tagawa et al. (2021b). The former is because the profile is characterized by the few parameters ( $m_{\text{max}}$ ,  $a_{\text{uni}}$ ,  $a_{\text{ave}}$ ) as found in § 3.1, while the latter is because the  $m_{\text{chirp}}$  distributions are affected by how BHs pair with other BHs and merge in AGN disks.

In this section, we additionally consider the spin distributions for mergers typically expected in several environments, including GCs, FBs, and MTs of AGN disks. Values of the parameters adopted to mimic these populations are listed in Table 3. Figs. 2 and 3, and panel (i) in Fig. 1 present the distributions and the profiles of the spin parameters ( $\chi_{\text{typ}}$ ,  $\chi_{\text{p}}$ , and  $\chi_{\text{eff}}$ ) as functions of  $m_{\text{chirp}}$  for these populations. Fig. 4 is the same as Fig. 3, but mergers are contributed by a mixture of two populations. Some contribution from multiple populations to the observed events is also favored by the analysis in Zevin et al. (2020b).

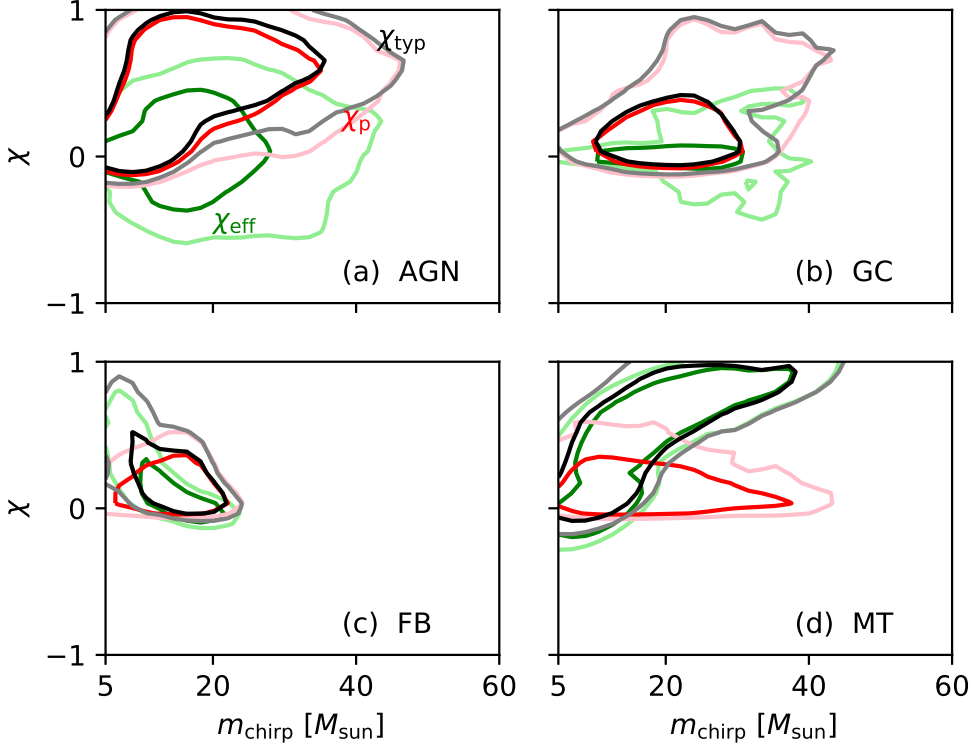


**Figure 2.** The 90 (dark lines) and 99 (light lines) percentile distributions in the spin  $\chi$  vs.  $m_{\text{chirp}}$  plane. Black, red, and green lines represent the distributions of  $\chi_{\text{typ}}$ ,  $\chi_p$ , and  $\chi_{\text{eff}}$ , respectively. Panels (a), (b), (c), and (d) show distributions for mergers in AGNs (bulk disks), GCs, FBs, and MTs, respectively.

For mergers in GCs, we set lower escape velocity  $v_{\text{esc}} = 30 \text{ km/s}$ ,  $N_s = 2$  and  $\omega = 0.03$  to reproduce the detection fraction of hierarchical mergers of  $\sim 10\text{--}20\%$ , which is predicted by theoretical studies (e.g. O’Leary et al. 2016; Rodriguez et al. 2019, Table 2). We chose higher  $m_{\text{max}} = 45 \text{ M}_\odot$  as GCs are composed of metal-poor stars (e.g. Peng et al. 2006; Leaman et al. 2013; Brodie et al. 2014); other parameters are the same as those for AGN disks.

Due to higher  $m_{\text{max}}$ ,  $\bar{\chi}_{\text{typ}}$  continues to increase until higher  $m_{\text{chirp}}$  (panel b in Fig. 3, see also Rodriguez et al. 2018) compared to the fiducial model (panel a). Also, 90 percentile regions are distributed around  $\chi_{\text{eff}} \sim 0$  and  $\chi_p \sim 0$  (Fig. 2 b) as a large fraction of mergers are among 1g BHs. Thus, the distribution of  $\bar{\chi}_{\text{typ}}$  at low  $m_{\text{chirp}}$  is clearly different between mergers in AGN disks and GCs, mainly due to the difference of  $m_{\text{max}}$  and the fraction of mergers among high-g BHs. If mergers are comparably contributed both by GCs and AGN disks, steep increase of  $\bar{\chi}_{\text{typ}}$  against  $m_{\text{chirp}}$  appears twice (panel a in Fig. 4). Thus, mixture of these populations can be discriminated by analyzing the spin distribution. Note that the intermediate line between the two increases in the  $\bar{\chi}_{\text{typ}}$  profile is roughly characterized by the ratio of mergers from AGN disks and GCs. Hence, the contribution from multiple populations would be distinguishable by analyzing the profile by using a number of GW events.

For mergers among FBs, we set  $N_s = 1$  and  $m_{\text{max}} = 30 \text{ M}_\odot$ . Although BH spin distributions are highly uncertain, we refer to Bavera et al. (2019) who proposed that  $\bar{\chi}_{\text{eff}}$  is high at low  $m_{\text{chirp}}$  of  $\lesssim 10 - 15 \text{ M}_\odot$  as low-mass

progenitors have enough time to be tidally spun up. We assume that  $a_{\text{uni}}$  follows

$$a_{\text{uni}} = \begin{cases} 1 & \text{for } m_{1g} \leq 10 \text{ M}_\odot \\ (20 \text{ M}_\odot - m_{1g})/10 \text{ M}_\odot & \text{for } 10 \text{ M}_\odot \leq m_{1g} \leq 20 \text{ M}_\odot \\ 0 & \text{for } 20 \text{ M}_\odot \leq m_{1g}. \end{cases} \quad (28)$$

BH spins are assumed to be always aligned with the orbital angular momentum of binaries, although we do not always expect spins to be aligned (e.g. Kalogera 2000; Rodriguez et al. 2016b). In such a setting,  $|\chi_{\text{eff}}|$  decreases as  $m_{\text{chirp}}$  increases (panels c of Figs. 2 and 3). The profile expected for the binary evolution channel is significantly different from those expected for the other channels. If mergers arise comparably from FBs and dynamical environments,  $|\chi_{\text{eff}}|$  exceeds  $\bar{\chi}_p$  at low  $m_{\text{chirp}}$  (panels b and c of Fig. 4). As contribution from mergers in FBs enhances  $|\chi_{\text{eff}}|$  relative to  $\bar{\chi}_p$  at low  $m_{\text{chirp}}$ , we could constrain the contribution from FBs using the ratio of  $|\chi_{\text{eff}}|$  to  $\bar{\chi}_p$ . Observed events so far suggest that  $|\chi_{\text{eff}}|$  is typically lower than  $\chi_p$  at low  $m_{\text{chirp}}$  (panel e of Fig. 3), implying that the contribution to the observed mergers from FBs is minor, unless adopted spins for 1g BHs need significant revisions.

For mergers in MTs, we assume that parameters are the same as in the fiducial model (Table 1), while BH spins are always aligned with the orbital angular momentum of the binaries. Such alignment is expected for binaries in MTs where randomization of the binary orbital

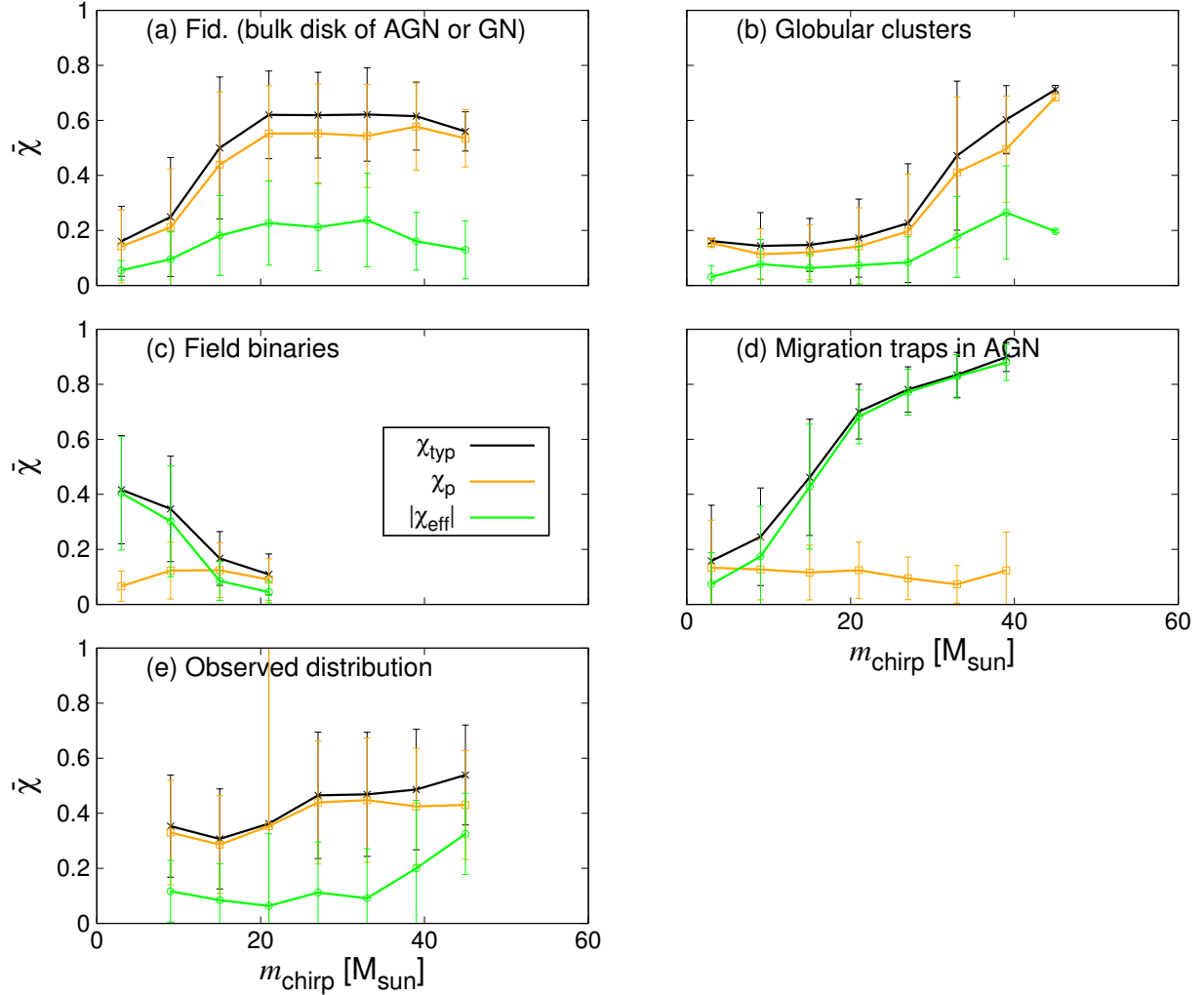


**Figure 3.** The profiles for the average spin parameters as a function of  $m_{\text{chirp}}$  for  $10^3$  detectable mergers. Black, orange, and green lines represent the average of  $\chi_{\text{typ}}$ ,  $\chi_p$ , and  $|\chi_{\text{eff}}|$ , respectively. Panels (a)–(e), respectively, present the distributions for mergers in AGN disks (M1), GCs (M25), FBs (M26), MTs (M27), and those observed by LIGO/Virgo O1–O3a. The averages for observed distributions (e) are calculated by averaging the medians of the parameters estimated in observed events. Bars correspond to  $1\sigma$  credible intervals.

angular momentum directions by binary-single interactions is inefficient due to rapid hardening and merger caused by gas dynamical friction (unlike in gaps formed further out in the disk, where these interactions were found to be very important by Tagawa et al. 2020a), and so the BH spins are aligned with circumbinary disks due to the Bardeen-Petterson effect (Bardeen & Petterson 1975), and circumbinary disks are aligned with the binaries due to viscous torque (e.g. Moody et al. 2019). Here, we assume that the orbital angular momentum directions of binaries are the same as that of the AGN disk referring to Lubow et al. (1999), which is different from the assumption (anti-alignment with 50%) adopted in Yang et al. (2019). In this model, the  $\chi_p$  and  $|\chi_{\text{eff}}|$  distributions are significantly different from those in the other models (panels d of Fig. 2 and Fig. 3). The value of  $\chi_{\text{eff}}$  at high  $m_{\text{chirp}}$  is typically high, while  $\chi_p$  is low. When mergers originate comparably in MTs and GCs,  $|\chi_{\text{eff}}|$  significantly exceeds  $\bar{\chi}_p$  in a wide range of  $m_{\text{chirp}}$  (panel d of Fig. 4). As  $|\chi_{\text{eff}}|$  is typically lower than  $\bar{\chi}_p$

the observed events in all  $m_{\text{chirp}}$  bins (panel e of Fig. 4), the contribution from MTs to the detected mergers is probably minor.

### 3.2. Application to LIGO/Virgo O1–O3a data

#### 3.2.1. Reconstruction of spin profiles

We analyze the GW data observed in LIGO/Virgo O1–O3a reported by Abbott et al. (2019b) and Abbott et al. (2020b). Fig. 5 presents the observed distributions of  $\chi_p$ ,  $\chi_{\text{eff}}$ , and  $\chi_{\text{typ}}$  as a function of  $m_{\text{chirp}}$ . Although  $\chi_p$  and  $\chi_{\text{typ}}$  suffer large uncertainties, their median values indicate a positive correlation with  $m_{\text{chirp}}$ . Such positive correlation is, if confirmed, consistent with the growth of BH spin magnitudes by hierarchical mergers as presented in Figs. 1 and 3.

To confirm the features in the  $\chi$ -profiles due to hierarchical mergers, we reconstruct the  $\bar{\chi}_{\text{typ}}$  profile from the observed GW data in the way described in § 2.3. For simplicity, we assume that errors on observables follow independent normal distributions, as assumed in stud-

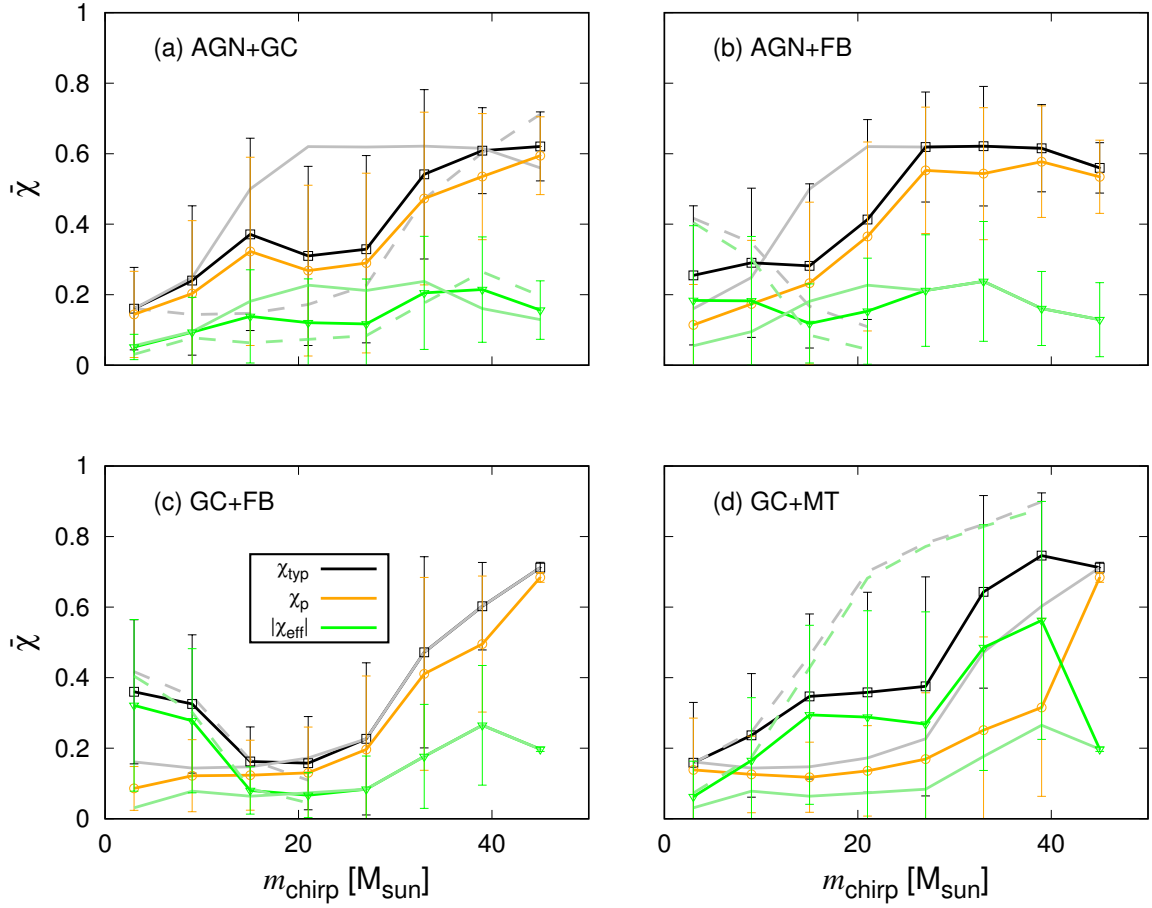


**Figure 4.** Same as Fig. 3, but for mixture of two models. Both channels contribute to 1000 mergers, and contributing two models are specified in the upper left of each panel. ”AGN”, ”GC”, ”FB”, and ”MT” represent mergers in the AGN disks, GCs, FBs, and MTs, respectively. Thin and dashed lines present the  $\chi_{\text{eff}}$  and  $\chi_{\text{typ}}$  profiles only for the former and the latter populations in the legend, respectively.

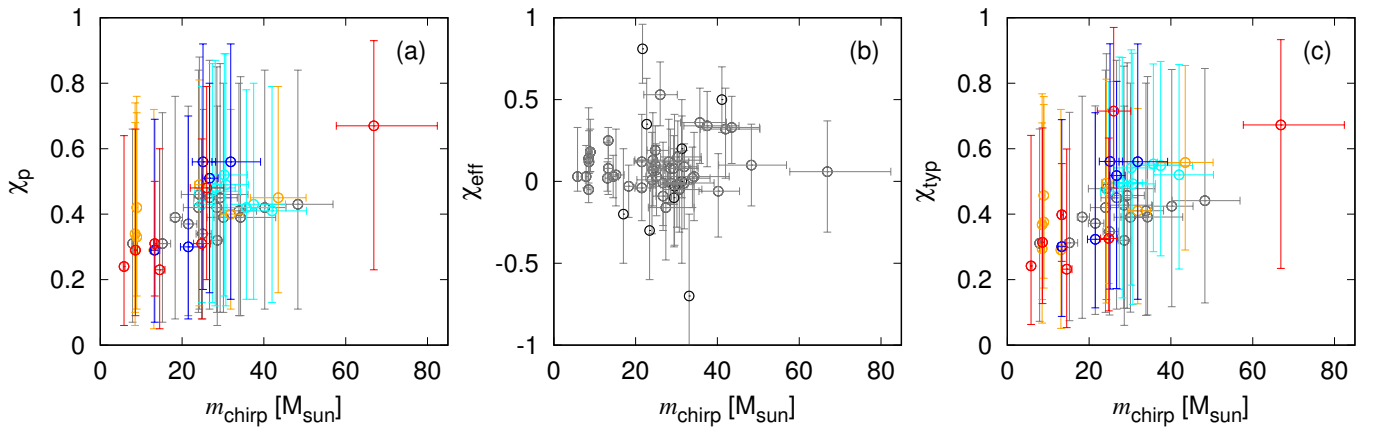


**Figure 5.** Observed distribution for spins reported in LIGO/Virgo O1–O3a. Panels (a)–(c) represent the distributions of  $\chi_p$ ,  $\chi_{\text{eff}}$ , and  $\chi_{\text{typ}}$ , respectively. Red, blue, orange, cyan, and gray circles represent events with the KL divergence between prior and posterior samples for  $\chi_p$  to be  $D_{\text{KL}} \geq 0.2$ ,  $0.2 > D_{\text{KL}} \geq 0.15$ ,  $0.15 > D_{\text{KL}} \geq 0.1$ ,  $0.1 > D_{\text{KL}} \geq 0.05$ , and  $0.05 > D_{\text{KL}}$ , respectively. Bars correspond to the 90 percentile credible intervals.

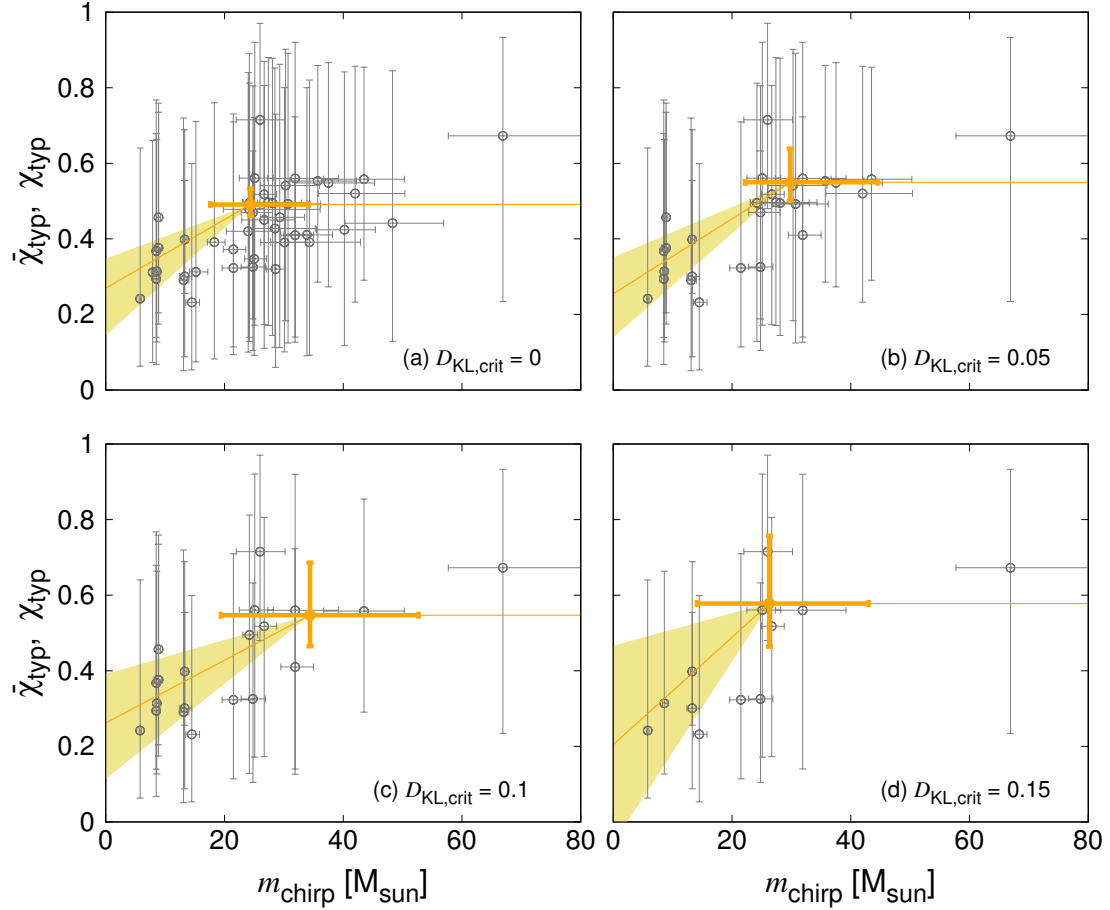


**Figure 6.** The  $\bar{\chi}_{\text{typ}}$  profile as a function of  $m_{\text{chirp}}$  constructed using the GW data observed in LIGO/Virgo O1–O3a. Orange line presents the recovered profile using the model described in § 2.3 (Eq. 15). Bars and shaded regions represent 1 $\sigma$  credible intervals for  $\bar{\chi}_{\text{typ}}$  at the plateau  $b_\mu$ , the critical chirp mass at the bending point of the profile  $m_{\text{crit},\mu}$ , and the slope of the  $\bar{\chi}_{\text{typ}}$  at a lower chirp mass  $a_\mu$ . Panels (a), (b), (c), and (d) presents results for events with  $D_{\text{KL}} \geq 0, 0.05, 0.1$ , and  $0.15$ , respectively. Gray plots are the same as those in Fig. 5 (c).

ies analyzing observed GW data (e.g. Fishbach & Holz 2017):

$$P(\mathbf{d}_i | m_{\text{chirp}}, \chi_{\text{eff}}, \chi_p) \simeq N(\bar{m}_{\text{chirp},i}, \sigma_{m_{\text{chirp},i}}^2) N(\bar{\chi}_{\text{eff},i}, \sigma_{\chi_{\text{eff},i}}^2) N(\bar{\chi}_{p,i}, \sigma_{\chi_{p,i}}^2), \quad (29)$$

where  $N(c_1, c_2^2)$  is the normal distribution with average  $c_1$  and dispersion  $c_2^2$ ,  $\bar{m}_{\text{chirp},i}$ ,  $\bar{\chi}_{\text{eff},i}$  and  $\bar{\chi}_{p,i}$  are the median values and  $\sigma_{m_{\text{chirp},i}}^2$ ,  $\sigma_{\chi_{\text{eff},i}}^2$ , and  $\sigma_{\chi_{p,i}}^2$  are the dispersions of  $m_{\text{chirp}}$ ,  $\chi_{\text{eff}}$ , and  $\chi_p$  observed in the  $i^{\text{th}}$  GW event. We set the average values for each event to the median values estimated in Abbott et al. (2020b), Abbott et al. (2019b), and Gerosa et al. (2020a). To take into account the asymmetry of errors found by the above authors, we use the standard deviation by the difference between the median and the 10 or 90% credible interval divided by 1.64 for ranges below and above the median values, respectively, with 50% probabilities. Note that the Gaussian assumption for the error distribution is not accurate, which should be revised in the future analysis. On the other hand, the posterior distribution for  $\chi_p$  estimated in Gerosa et al. (2020a) looks similar to the Gaussian distribution, which may justify the assumption.

We only use the events listed in Gerosa et al. (2020a), and adopt the values for  $\chi_p$  in the column ‘‘Heuristic’’ of Table 1 in Gerosa et al. (2020a). However, the prior and posterior distributions for some events listed in Gerosa et al. (2020a) are similar to each other, which means that  $\chi_p$  is less constrained by the waveforms. To exclude events in which  $\chi_p$  are not well estimated, we only use events in which the Kullback-Leibler (KL) divergence between prior and posterior samples evaluated using heuristic estimates of  $\chi_p$  ( $D_{\text{KL}}$ ) exceeds a critical value of  $D_{\text{KL,cri}} = 0, 0.05, 0.1, 0.15$ , or  $0.2$ . We consider that  $\chi_p$  for events with non-zero  $D_{\text{KL}}$  is statistically useful to understand the spin distribution. Here, we do not use GW190814 below since we only model mergers among BHs while a plausible explanation for GW190814 is a merger of a massive (possibly collapsed) NS or a merged remnant of NSs (or some other objects). Then, the number of events with  $D_{\text{KL}} \geq 0, 0.05, 0.1, 0.15$ , and  $0.2$  are  $43, 28, 20, 12$ , and  $7$ , respectively. We present  $1\sigma$  errors on the estimated parameters below unless stated otherwise.

The reconstructed  $\bar{\chi}_{\text{typ}}$  profiles for  $D_{\text{KL,cri}} = 0, 0.05, 0.1$ , and  $0.15$  are, respectively, presented by orange lines in panels (a)–(d) of Fig. 6. Note that for  $D_{\text{KL,cri}} = 0.2$ , parameters are not well determined due to the small number of events. For  $D_{\text{KL,cri}} = 0, 0.05, 0.1$ , and  $0.15$ , respectively,  $\bar{\chi}_{\text{typ}}$  at the plateau is  $b_\mu = 0.49^{+0.04}_{-0.03}, 0.55^{+0.09}_{-0.05}, 0.55^{+0.14}_{-0.08}$ , and  $0.58^{+0.18}_{-0.11}$ , the critical chirp mass at the bending point of the  $\bar{\chi}_{\text{typ}}$  profile is  $m_{\text{crit},\mu} = 24^{+10}_{-6} \text{ M}_\odot, 30^{+15}_{-8} \text{ M}_\odot, 34^{+19}_{-15} \text{ M}_\odot$ , and  $26^{+17}_{-12} \text{ M}_\odot$ , and the slope of  $\bar{\chi}_{\text{typ}}$  at  $m_{\text{chirp}} < m_{\text{crit},\mu}$  is  $a_\mu = 9^{+3}_{-3} \times 10^{-3} \text{ M}_\odot^{-1}, 10^{+4}_{-3} \times 10^{-3} \text{ M}_\odot^{-1}, 8^{+5}_{-3} \times 10^{-3} \text{ M}_\odot^{-1}$ , and  $14^{+10}_{-10} \times 10^{-3} \text{ M}_\odot^{-1}$ .

The positive value of the slope ( $a_\mu$ ), i.e., the increase of  $\bar{\chi}_{\text{typ}}$  at low  $m_{\text{chirp}}$  is confirmed with  $\gtrsim 2\sigma$  confidence for  $D_{\text{KL,cri}} \leq 0.1$  and  $\sim 1\text{--}2\sigma$  confidence for  $D_{\text{KL,cri}} = 0.15$ , which is a tell-tale sign of frequent hierarchical mergers. Also, according to the analysis in § 3.1, the detection of the rise of  $\bar{\chi}_{\text{typ}}$  at low  $m_{\text{chirp}}$  with  $N_{\text{obs}} = 50$  roughly requires that the detection fraction of mergers of high-g

BHs exceeds  $\sim 0.15$ . As the number of events is smaller than 50 (e.g.  $N_{\text{obs}} = 28$  for  $D_{\text{KL,cri}} = 0.05$ ), the high-g detection fraction would be even higher than  $\sim 0.15$ . Thus, hierarchical mergers are preferred from the analysis. Note that accretion can also produce a positive correlation, but  $|\chi_{\text{eff}}| > \chi_p$  is predicted in such cases, similarly to mergers in MTs (panel d of Fig. 3). As  $|\chi_{\text{eff}}| < \chi_p$  is predicted by GW observations (panel e of Fig. 3), accretion is disfavored as a process enhancing the BH spin magnitudes.

For  $D_{\text{KL,cri}} = 0.05, 0.1$ , and  $0.15$  (panels b, c, and d of Fig. 6), the value of  $\bar{\chi}_{\text{typ}}$  at the plateau ( $b_\mu \sim 0.6$ ) is consistent with that expected from hierarchical mergers ( $\sim 0.6$ ), which possibly supports frequent hierarchical mergers with the high-g detection fraction to be  $\gtrsim 0.5$  (§ 3.1.1). On the other hand, for  $D_{\text{KL,cri}} = 0$ ,  $b_\mu \sim 0.5$ , which is somewhat lower than the expected value of 0.6. This is presumably because  $\chi_p$  values for events with  $D_{\text{KL}} \leq 0.05$  are not well constrained and just reflect assumed priors. Also, note that events with high  $\chi_p$  might tend to be missed as the waveform for large  $\chi_p$  (Apostolatos et al. 1994; Kidder 1995; Pratten et al. 2020) or spin (Kesden et al. 2010; Gerosa et al. 2019) mergers often accompany strong amplitude modulation, reducing SNRs.

Here,  $\bar{\chi}_{\text{typ}}$  at  $m_{\text{chirp}} = m_{\text{min}}$  is closely related to the typical spin magnitude for 1g BHs (Fig. 1 e). If we assume the median values for  $\bar{\chi}_{\text{typ}}$  and  $m_{\text{crit},\mu}$ ,  $\bar{\chi}_{\text{typ}}$  at  $m_{\text{chirp}} = 5 \text{ M}_\odot$  is  $0.31^{+0.06}_{-0.09}, 0.30^{+0.08}_{-0.09}, 0.30^{+0.11}_{-0.12}$ , and  $0.28^{+0.21}_{-0.22}$  for  $D_{\text{KL,cri}} = 0, 0.05, 0.1$ , and  $0.15$ , respectively. These suggest that 1g BHs typically have  $a \lesssim 0.4$ . Since this value is effectively enhanced by the observational errors on  $\bar{\chi}_p$ , the estimated typical spin magnitude of 1g BHs is still consistent with  $\sim 0$  as predicted by stellar evolution models (Fuller & Ma 2019), which is also verified later (§ 3.3).

The critical chirp mass at the bending point of the  $\bar{\chi}_{\text{typ}}$  profile ( $m_{\text{crit},\mu}$ ) is related to the maximum mass of 1g BHs (Fig. 1 f). The analysis loosely constrains the parameter to  $m_{\text{crit},\mu} \sim 15\text{--}50 \text{ M}_\odot$ , from which we discuss in § 3.3 that the maximum mass of 1g BHs is estimated to be  $\sim 20\text{--}60 \text{ M}_\odot$ . However, it needs a caution that  $m_{\text{crit},\mu}$  is restricted from  $5 \text{ M}_\odot$  to the maximum chirp mass among the event ( $\sim 67 \text{ M}_\odot$ ) in this analysis, which may artificially produce the bending point and the plateau. To confidently confirm the plateau,  $m_{\text{crit},\mu}$  needs to be precisely constrained compared to the allowed range for  $m_{\text{crit},\mu}$  of  $5\text{--}67 \text{ M}_\odot$ , which would require further events (see also § 3.3).

### 3.2.2. Bayes factors on spins and mass distributions

In the previous section we focus on the  $\bar{\chi}_{\text{typ}}$  profile, while here we use the distributions of  $\chi_{\text{eff}}$ ,  $\chi_p$ , and  $m_{\text{chirp}}$  and discuss the preferred values for underlying parameters  $\lambda_0$ .

To assess the relative likelihood to produce each event in different models, we calculate the Bayes factors between pairs of models,

$$K_{\text{A,B}} = \frac{P(\mathbf{d}|A)}{P(\mathbf{d}|B)} \quad (30)$$

**Table 4**

The parameters of model A which are different from each population model (shown in Table 3) and the logarithm of their Bayes factor  $K_{A,B}$  relative to the fiducial model ("B"). The Bayes factors for the three parameters with  $D_{KL,cri} = 0, 0.05, 0.1, 0.15$ , and  $0.2$ , and that for the two parameters are presented from the second to seventh columns. We highlight the models with positive Bayes factors in the five rightmost columns in boldface.

Parameters	$\log_{10} K_{A,B}$ in 3D					$\log_{10} K_{A,B}$ in 2D
	$D_{KL,cri} = 0$	$D_{KL,cri} = 0.05$	$D_{KL,cri} = 0.1$	$D_{KL,cri} = 0.15$	$D_{KL,cri} = 0.2$	-
AGN disk or NSC						
$m_{\max} = 15 M_{\odot}$	-6.9	-3.9	-1.8	-2.1	-1.0	-9.3
$m_{\max} = 25 M_{\odot}$	0.49	-0.43	-1.3	-0.70	-0.46	<b>1.7</b>
$m_{\max} = 30 M_{\odot}$	-1.3	-2.0	-3.0	-1.4	-0.95	<b>0.14</b>
$m_{\max} = 35 M_{\odot}$	-4.0	-4.2	-4.9	-2.6	-1.6	-0.40
$m_{\max} = 45 M_{\odot}$	-8.8	-7.8	-7.7	-4.2	-2.5	-6.8
$\alpha = 2$	-0.40	<b>0.48</b>	<b>0.94</b>	<b>0.19</b>	<b>0.48</b>	<b>0.020</b>
$\alpha = 2, m_{\max} = 15 M_{\odot}$	-14	-7.3	-5.7	-4.4	-3.3	-18
$\alpha = 2, m_{\max} = 25 M_{\odot}$	1.4	<b>1.1</b>	<b>0.47</b>	-0.083	<b>0.17</b>	<b>1.7</b>
$\alpha = 2, m_{\max} = 30 M_{\odot}$	1.3	<b>0.30</b>	-0.71	-0.58	-0.22	<b>3.0</b>
$\alpha = 2, m_{\max} = 35 M_{\odot}$	-0.22	-0.97	-1.7	-0.96	-0.38	<b>0.41</b>
$\alpha = 2, m_{\max} = 45 M_{\odot}$	-3.1	-3.1	-3.4	-2.0	-0.93	-0.30
$a_{\text{uni}} = 1$	-1.8	-1.3	-1.7	-1.3	-0.91	-0.19
$a_{\text{ave}} = 0.3$	0.91	<b>1.1</b>	<b>0.72</b>	<b>0.21</b>	<b>0.17</b>	<b>0.90</b>
$a_{\text{ave}} = 0.5$	-1.2	-0.41	-0.60	-0.86	-0.45	-0.13
$a_{\text{ave}} = 0.7$	-5.3	-3.4	-3.7	-2.5	-1.7	-1.7
$\sigma_p = 0.3$	-0.31	<b>0.088</b>	<b>0.063</b>	-0.13	-0.036	<b>0.27</b>
$\sigma_p = 0.4$	0.47	<b>0.30</b>	-0.026	-0.12	-0.12	<b>1.5</b>
$v_{\text{esc}} = 30 \text{ km/s}$	-15	-8.8	-4.7	-6.8	-8.5	-15
$w = 0.03$	-31	-18	-10	-12	-5.8	-42
$w = 0.2$	-3.2	-2.4	-2.9	-1.7	-0.73	-1.4
$\gamma_t = 0$	-24	-13	-11	-7.8	-9.6	-34
$\gamma_t = 4$	-3.9	-2.9	-3.0	-1.7	-0.57	-2.6
$\gamma_q = 0$	-5.6	-4.4	-1.6	-2.2	-1.7	-9.4
$\gamma_q = 4$	0.45	<b>0.059</b>	-0.23	-0.086	-0.049	<b>1.3</b>
$N_s = 2$	-50	-33	-26	-24	-18	-40
$N_s = 2, m_{\max} = 30 M_{\odot}$	-1.5	-3.7	-4.8	-2.8	-3.6	-3.4
$N_s = 2, m_{\max} = 45 M_{\odot}$	-4.9	-6.6	-7.8	-4.2	-3.1	-5.0
$N_s = 2, m_{\max} = 60 M_{\odot}$	-15	-13	-13	-7.0	-4.7	-19
$N_s = 3$	-4.6	-2.9	-2.4	-1.6	-1.3	-6.5
$N_s = 3, m_{\max} = 25 M_{\odot}$	0.74	-0.27	-1.2	-0.46	-0.66	<b>0.71</b>
$N_s = 3, m_{\max} = 30 M_{\odot}$	1.2	-0.63	-1.8	-0.75	-0.72	<b>3.9</b>
$N_s = 3, m_{\max} = 35 M_{\odot}$	-0.93	-2.8	-4.1	-2.0	-1.8	<b>1.3</b>
$N_s = 3, m_{\max} = 45 M_{\odot}$	-7.9	-7.5	-7.8	-4.3	-3.0	-7.1
$N_s = 5$	0.26	<b>0.13</b>	-0.30	-0.27	<b>0.21</b>	<b>0.54</b>
$N_s = 5, m_{\max} = 15 M_{\odot}$	-0.78	<b>0.017</b>	<b>0.28</b>	-0.49	<b>0.057</b>	<b>0.0081</b>
$N_s = 5, m_{\max} = 30 M_{\odot}$	-3.7	-3.4	-3.6	-2.0	-0.96	-3.0
$N_s = 5, m_{\max} = 45 M_{\odot}$	-11	-8.5	-7.7	-4.4	-2.3	-9.6
$N_s = 6$	-2.8	-1.7	-2.1	-1.2	-0.32	-1.1
Globular cluster						
Fiducial	-17	-16	-15	-8.4	-6.1	-21
$\alpha = 2$	-2.9	-4.1	-5.0	-5.9	-3.5	-6.6
$m_{\max} = 30 M_{\odot}$	-14	-8.9	-9.6	-7.9	-9.3	-24
$a_{\text{uni}} = 1$	-12	-13	-16	-9.9	-9.4	-8.3
$a_{\text{ave}} = 0.3$	-0.16	-4.6	-7.3	-4.5	-5.0	-17
$a_{\text{ave}} = 0.5$	-1.4	-4.1	-7.8	-4.1	-4.7	-5.6
$a_{\text{ave}} = 0.7$	-12	-11	-13	-8.3	-8.1	-7.7
$v_{\text{esc}} = 100 \text{ km/s}$	-5.3	-8.8	-9.4	-5.3	-4.8	-20
$w = 0.05$	-3.4	-7.3	-8.1	-4.2	-3.8	-2.6
$w = 0.1$	-4.5	-6.6	-8.1	-4.1	-3.4	-2.7
$\alpha = 2, a_{\text{uni}} = 1$	-2.4	-4.6	-5.2	-3.6	-4.5	-0.60
$\alpha = 2, a_{\text{ave}} = 0.3$	4.3	-0.11	-0.91	-1.3	-2.3	-8.7
$\alpha = 2, a_{\text{ave}} = 0.5$	0.49	-1.2	-5.0	-4.2	-4.2	-4.8
Field binary						
Fiducial	-107	-105	-85	-71	-60	-220
Migration trap						
Fiducial	-62	-31	-21	-17	-8.3	-120
AGN disk (Tagawa et al. 2021b)						
$f_{\text{m1g}} = 1$	-4.0	-2.5	-1.3	-1.5	-0.26	-3.2
$f_{\text{m1g}} = 1.33$	-2.6	-2.0	-1.4	-0.88	-0.33	-1.8
$f_{\text{m1g}} = 1.66$	1.8	<b>2.0</b>	<b>2.1</b>	<b>3.2</b>	<b>3.5</b>	-0.88
$f_{\text{m1g}} = 2$	0.95	-0.18	-0.82	-0.20	-0.078	<b>2.7</b>
$f_{\text{m1g}} = 3$	2.7	-0.41	-2.1	-1.9	-1.2	<b>4.3</b>

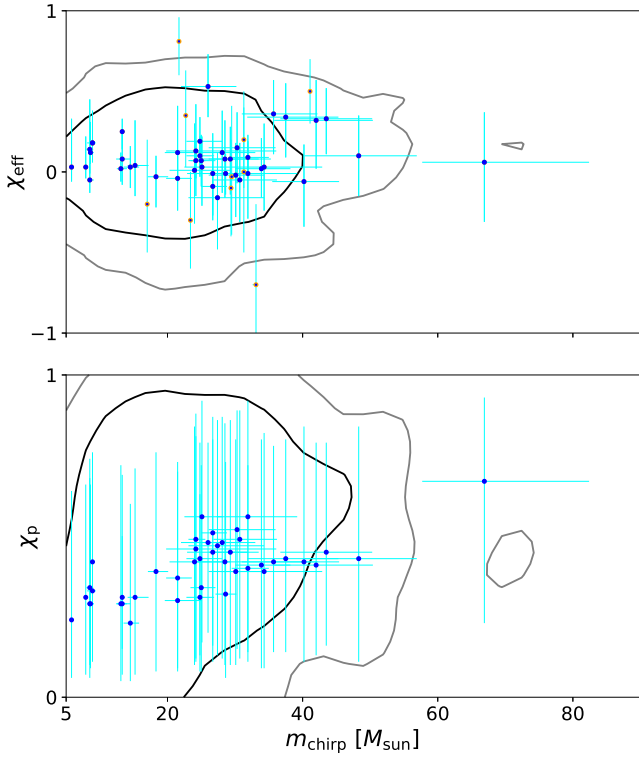


**Figure 7.** Comparisons between the  $\chi_{\text{eff}}$  (upper) or  $\chi_p$  (lower) and  $m_{\text{chirp}}$  distributions observed by LIGO/Virgo O1–O3a and those predicted by the model with  $m_{\text{max}} = 30 M_{\odot}$  and  $\alpha = 2$  which have high Bayes factors (Table 4). Black and gray lines correspond to 90 and 99 credible intervals for the predicted distributions, and cyan bars correspond to the 90 percentile credible intervals for the observed variables. The blue and orange points in the upper panel corresponds to the events in which  $\chi_p$  are estimated in Gerosa et al. (2020a) or not, respectively.

where

$$P(\mathbf{d}|A) = \prod_i P(\mathbf{d}_i|A), \quad (31)$$

$P(\mathbf{d}_i|A)$  is the likelihood of obtaining data  $\mathbf{d}_i$  observed in the GW event  $i$  from model  $A$ ,

$$P(\mathbf{d}_i|A) = \int P(\mathbf{d}_i|m_{\text{chirp}}, \chi_{\text{eff}}, \chi_p) P(m_{\text{chirp}}, \chi_{\text{eff}}, \chi_p|A) dm_{\text{chirp}} d\chi_{\text{eff}} d\chi_p \quad (32)$$

and  $P(m_{\text{chirp}}, \chi_{\text{eff}}, \chi_p|A)$  is the probability distribution of  $m_{\text{chirp}}$ ,  $\chi_{\text{eff}}$ , and  $\chi_p$  in model  $A$ . We calculate the three dimensional likelihood  $P(\mathbf{d}_i|m_{\text{chirp}}, \chi_{\text{eff}}, \chi_p)$  for the events listed in Gerosa et al. (2020a).

We calculate the Bayes factors for events with  $D_{\text{KL}} \geq D_{\text{KL,crit}} = 0, 0.05, 0.1, 0.15$ , and  $0.2$ . We consider  $D_{\text{KL,crit}} = 0.05$  as the fiducial value, and mostly discuss the Bayes factors for  $D_{\text{KL,crit}} = 0.05$  below. Note that the events with positive Bayes factors for  $D_{\text{KL,crit}} = 0.1, 0.15$ , or  $0.2$  always have positive Bayes factors also for  $D_{\text{KL,crit}} = 0.05$  somewhat incidentally.

To calculate  $P(m_{\text{chirp}}, \chi_{\text{eff}}, \chi_p|A)$ , we first count mergers in  $30 \times 30 \times 30$  uniform bins in  $\chi_{\text{eff}}$ ,  $m_{\text{chirp}}$ , and  $\chi_p$  for

model  $A$ . The maximum and minimum values of  $m_{\text{chirp}}$  for the bins are set to  $100$  and  $5 M_{\odot}$ , respectively. In this section, we generate 1000 mergers for each model. To include error distributions for the variables ( $m_{\text{chirp}}$ ,  $\chi_{\text{eff}}$ ,  $\chi_p$ ) to  $P(m_{\text{chirp}}, \chi_{\text{eff}}, \chi_p|A)$ , we sample 10 different realizations for each merger event predicted by the model. To reduce the statistical fluctuation in the distribution of  $\chi_{\text{eff}}$ ,  $m_{\text{chirp}}$ , and  $\chi_p$  due to the finite number of mergers in our models, we perform a kernel-density estimate for the distribution using Gaussian kernels whose bandwidth is chosen to satisfy the Scott's Rule (Scott 1992). We calculate  $P(\mathbf{d}_i|m_{\text{chirp}}, \chi_{\text{eff}}, \chi_p)$  by means of 300 samples generated according to the observed error distribution (Eq. 29) as used in the previous section.

For reference, we also calculate the Bayes factors for the two parameters,  $m_{\text{chirp}}$  and  $\chi_{\text{eff}}$ , using the 54 events reported in Abbott et al. (2019b), Zackay et al. (2019), and Abbott et al. (2020b) in the same way as that for three parameters (rightmost column in Table 4).

Table 4 lists the Bayes factors for some models relative to the fiducial model ( $= B$ , Table 1). The Bayes factors suggest that, compared to the  $m_{\text{chirp}}$ ,  $\chi_{\text{eff}}$ , and  $\chi_p$  distributions typically expected for mergers in FBs and MTs (Table 3), the observed distribution is much more consistent with those in AGN disks. This is because high  $|\chi_{\text{eff}}|$  and low  $\chi_p$  expected for mergers either in FBs or MTs (panels c and d in Figs. 2 and 3) are incompatible with the observed distribution of  $|\chi_{\text{eff}}| < \chi_p$  (Fig. 3 e).

For mergers in GCs, the models with small spin magnitudes for 1g BHs are less favored. This is presumably because infrequent hierarchical mergers ( $\lesssim 20\%$ ) in GCs are difficult to explain typically high values of  $\chi_p$  if 1g BHs have low spin magnitudes. On the other hand, for  $a_{\text{ave}} = 0.3$  and  $\alpha = 2$ , the Bayes factor for  $D_{\text{KL,crit}} = 0.05$  is as high as  $10^{-0.11}$ . Thus, if mergers originate from GCs, 1g BHs are favored to have high spin magnitudes and follow a bottom heavy initial mass function.

For mergers in AGN disks or NSCs, the models with non-zero values for initial BH spins ( $a_{\text{ave}} = 0.3$ ) as well as a high value for  $\sigma_{\chi_p}$  ( $\sim 0.3\text{--}0.4$ ) have high Bayes factors of  $10^{1.1}$  and  $10^{0.89}\text{--}10^{0.30}$  for  $D_{\text{KL,crit}} = 0.05$ , respectively. This is because non-zero  $\bar{\chi}_{\text{typ}}$  at low  $m_{\text{chirp}}$  in the observed distribution (Fig. 5) can be explained by adjusting these variables (Fig. 1). Also, large values for  $\alpha$ , which effectively shift the  $\chi_{\text{typ}}$  and  $m_{\text{chirp}}$  distribution toward lower  $m_{\text{chirp}}$ , and accordingly raises  $\bar{\chi}_{\text{typ}}$  at low  $m_{\text{chirp}}$  (e.g. Fig. 1 f). This is presumably the reason why the model with  $\alpha(= 2)$  has a high Bayes factor of  $10^{1.1}$  at  $m_{\text{max}} \sim 25 M_{\odot}$  compared to the models with  $\alpha = 1$  ( $K_{A,B} \lesssim 1$ ).

Preferred values for  $m_{\text{max}}$  are probably as low as  $\sim 15\text{--}30 M_{\odot}$  if the typical spin magnitude for 1g BHs is low. For  $\alpha = 1$ , in the models with  $N_s = 3, 4$ , and  $5$ , respectively,  $m_{\text{max}} = 25\text{--}30 M_{\odot}$ ,  $m_{\text{max}} = 20\text{--}25 M_{\odot}$ , and  $m_{\text{max}} = 15\text{--}20 M_{\odot}$  is preferred. The difference in preference of  $m_{\text{max}}$  for different  $N_s$  is because both variables are constrained by the maximum  $m_{\text{chirp}}$  among the GW events. In any case, the preferred values of  $m_{\text{max}} = 15\text{--}30 M_{\odot}$  are roughly consistent with the values estimated in the previous section.

We also compare the properties inferred from GW observations with those predicted for mergers in AGN disks, which are calculated from one-dimensional  $N$ -body simulations, combined with a semi-analytical model used in

Tagawa et al. (2021b). We adopt the fiducial model in Tagawa et al. (2021b), while we investigate several variations in which the initial BH masses are multiplied by  $f_{\text{m1g}} = 1, 1.33, 1.66, 2$ , and  $3$  so that  $m_{\text{max}} = 15, 20, 25, 30$ , and  $45 M_{\odot}$ , respectively. Since 1g BH masses are  $5\text{--}15 M_{\odot}$  in the fiducial model, the minimum BH mass is given by  $5f_{\text{m1g}} M_{\odot}$ , in which the minimum chirp mass is  $\sim 8.7f_{\text{m1g}} M_{\odot}$ . To eliminate a reduction of the likelihood due to the lack of 1g BHs in the low mass ranges, we here calculate Bayes factors only using events with  $m_{\text{chirp}} \geq 8.7f_{\text{m1g}} M_{\odot}$ . The errors on  $m_{\text{chirp}}$ ,  $\chi_{\text{eff}}$ , and  $\chi_p$  are simply given by the normal distribution with the standard deviation of  $0.08 m_{\text{chirp}}$ ,  $0.12$ , and  $0.2$ , respectively. The Bayes factors are listed in the bottom five rows in Table 4, which indicate that  $m_{\text{max}} \sim 25\text{--}30 M_{\odot}$  ( $f_{\text{m1g}} = 1.66\text{--}2$ ) is preferred.

Thus, the properties predicted for AGN disk-assisted mergers are likely to be consistent with the observed properties of the GW events.

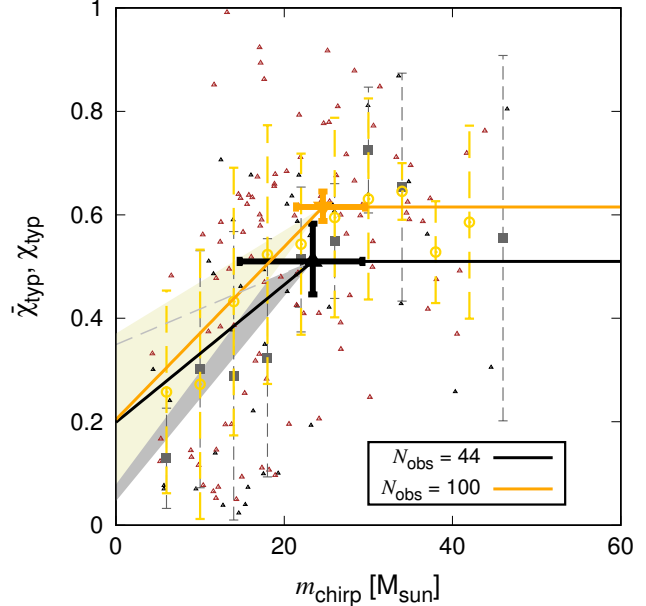
Here, events with high Bayes factors for  $D_{\text{KL,crit}} = 0.05$  tend to have high Bayes factors for the two dimensional likelihood (bold number in the third and rightmost columns of Table 4). We consider that this fact would further support the preferred models discussed above.

Fig. 7 compares the  $m_{\text{chirp}}$ ,  $\chi_{\text{eff}}$  and  $\chi_p$  distributions observed by LIGO/Virgo O1–O3a and those predicted by the model for the fiducial settings (Table 1) but  $m_{\text{max}} = 30 M_{\odot}$  and  $\alpha = 2$ , which is assessed to high Bayes factors for both  $D_{\text{KL,crit}} = 0.05$  and the two parameters (Table 4). We can see that the observed distribution for these variables (blue and orange points) roughly follows the 90 and 99 percentile regions (black and gray lines) predicted by the model.

Overall, our analyses suggest that  $m_{\text{max}} = 15\text{--}30 M_{\odot}$  with a high fraction of hierarchical mergers, or high spin magnitudes of  $\sim 0.3$  for 1g BHs is favored. The former may support mergers in NSCs including AGN disks, while the latter may be consistent with those in GCs. Further events would be required to assess these possibilities in more detail.

We also discuss the spin distribution suggested in The LIGO Scientific Collaboration et al. (2020c). First, we compare the average and the standard deviation of  $\chi_p$  predicted by models and those estimated from LIGO/Virgo O1–O3a data. By analyzing the observed GW data, The LIGO Scientific Collaboration et al. (2020c) estimated that the average and the standard deviation of  $\chi_p$  are  $0.21^{+0.15}_{-0.14}$  and  $0.09^{+0.21}_{-0.07}$ , respectively, assuming a truncated mass model. These values are consistent with models in which hierarchical mergers are frequent such as models M1, M6–M7, M11, M12, M15–M19 (Table 2). Also, the average and the standard deviation  $\chi_p$  for the model of GC with  $a_{\text{ave}} = 0.3$  is  $0.25$  and  $0.062$ , respectively, which are also consistent with the values estimated from the observed data. This fact further supports our claim that frequent hierarchical mergers or high spin magnitudes of  $\sim 0.3$  for 1g BHs is favored. Here, note that the dependence of the spins on masses expected from hierarchical mergers is taken into account in our analysis, which would be a critical difference from that in The LIGO Scientific Collaboration et al. (2020c).

Next, we discuss the fraction of mergers with positive and negative  $\chi_{\text{eff}}$ . The LIGO Scientific Collaboration et al. (2020c) analyzed the GW data observed in



**Figure 8.** The  $\bar{\chi}_{\text{typ}}$  profile as a function of  $m_{\text{chirp}}$  constructed using the mock GW data for 100 (orange), and 44 (black) observed events. Thick lines present the recovered profiles as in Fig. 6. The triangles corresponds to the median values of  $\chi_{\text{typ}}$  for all mock events. The dashed lines show  $1\sigma$  credible intervals for observed values of  $\bar{\chi}_{\text{typ}}$  for mock events.

LIGO/Virgo O1–O3a, and estimated that  $0.67^{+0.16}_{-0.16}$  (the 90% credible intervals) and  $0.27^{+0.17}_{-0.15}$  of mergers have  $\chi_{\text{eff}} > 0.01$  and  $\chi_{\text{eff}} < -0.01$ , respectively. In the fiducial model (Table 1), the fraction of mergers with  $\chi_{\text{eff}} > 0.01$  is  $0.54$  and that for  $\chi_{\text{eff}} < -0.01$  is  $0.41$ . The larger fraction for positive  $\chi_{\text{eff}}$  compared to that for negative one in the model is due to the assumed dependence of  $\rho_0$  on  $\chi_{\text{eff}}$  in Eq. (7). The fraction of mergers with negative  $\chi_{\text{eff}}$  in the model is somewhat higher than that estimated in The LIGO Scientific Collaboration et al. (2020c). Such difference may be due to large uncertainties for the estimated fraction, while it may suggest that the dependence of  $\rho_0$  on  $\chi_{\text{eff}}$  is stronger than that adopted in Eq. (7), or BH spins are moderately aligned toward the binary angular momentum directions due to interactions with gas, tidal synchronization, or alignment of spins for progenitor stars.

### 3.3. Reconstruction of the spin profile from mock GW data

We investigate how well the  $\bar{\chi}_{\text{typ}}$  profile can be reconstructed from mock GW data (§ 2.2.3) for different values of  $N_{\text{obs}}$  by performing the MCMC method as described in § 2.3. Fig. 8 shows  $\bar{\chi}_{\text{typ}}$  as a function of  $m_{\text{chirp}}$  for  $N_{\text{obs}} = 44$  (black) and  $N_{\text{obs}} = 100$  (orange) for the model with the fiducial setting (Table 1) but  $m_{\text{max}} = 30 M_{\odot}$  and  $\alpha = 2$ , which is preferred from observed GW events (§ 3.2.1 and § 3.2.2).

As the parameter estimate tends to be biased in small  $N_{\text{obs}}$ , we additionally perform 11 models for  $N_{\text{obs}} = 44$  with same settings with independent realizations of the initial condition. By averaging the estimated parameters for twelve models,  $\bar{\chi}_{\text{typ}}$  at the plateau is  $b_{\mu} = 0.62^{+0.09}_{-0.07}$  with the standard deviation  $\sigma(b_{\mu}) = 0.06$ , the critical

chirp mass is  $m_{\text{crit},\mu} = 27^{+7}_{-7} M_{\odot}$  with  $\sigma(m_{\text{crit},\mu}) = 4 M_{\odot}$ , and the slope of  $\bar{\chi}_{\text{typ}}$  in  $m_{\text{chirp}} < m_{\text{crit},\mu}$  is  $a_{\mu} = 19^{+9}_{-7} \times 10^{-3} M_{\odot}^{-1}$  with  $\sigma(b_{\mu}) = 6 \times 10^{-3} M_{\odot}^{-1}$ . As these uncertainties on the reconstructed parameters from the GW mock data are similar to those derived from the observed GW data in § 3.2.1, we conclude that the GW mock data are a useful tool to understand how well the spin profile can be reconstructed.

The critical chirp mass is estimated to be  $m_{\text{crit},\mu} = 25^{+5}_{-4} M_{\odot}$  for  $N_{\text{obs}} = 100$ , and  $m_{\text{crit},\mu} = 24.1^{+1.0}_{-0.9} M_{\odot}$  for  $N_{\text{obs}} = 1000$ . Here, the estimated value of  $m_{\text{crit},\mu}$  is lower than  $m_{\text{max}}$  by  $\sim 20\%$  mostly because  $m_{\text{chirp}} = (m_1 + m_2)[q(1+q)^{-2}]^{3/5} \lesssim 0.87 m_{\text{max}}$ . As the analysis on the observed GW events in § 3.2.1 derives  $m_{\text{crit},\mu} \sim 15-50 M_{\odot}$ ,  $m_{\text{max}} \sim 20-60 M_{\odot}$  is roughly inferred according to the relation of  $m_{\text{max}} \sim 1.2 m_{\text{crit},\mu}$ .

The average spin parameter  $\bar{\chi}_{\text{typ}}$  at  $m_{\text{chirp}} = m_{\text{min}}$  is related to the typical spin magnitude of 1g BHs (e.g. Fig. 1).  $\bar{\chi}_{\text{typ}}$  at  $m_{\text{chirp}} = 5 M_{\odot}$  is  $0.27^{+0.11}_{-0.12}$  for  $N_{\text{obs}} = 44$ , and  $0.29^{+0.13}_{-0.10}$  for  $N_{\text{obs}} = 100$ . These values derived from the model with  $a_{\text{ave}} = a_{\text{uni}} = 0$  are similar to the value ( $\sim 0.3 \pm \sim 0.1$ ) derived from the observed GW data (§ 3.2.1), suggesting that the typical spin magnitude of 1g BHs inferred from the observed GW events is still consistent with  $\sim 0$ .

For  $N_{\text{obs}} = 100$ ,  $\bar{\chi}_{\text{typ}}$  at the plateau is  $b_{\mu} = 0.62^{+0.03}_{-0.03}$ , which is similar to the expected value for hierarchical mergers ( $\sim 0.6$ , § 3.1.1). Also, the mass at the bending point is well constrained with  $N_{\text{obs}} = 100$  as mentioned above. Thus, with  $N_{\text{obs}} \geq 100$ , parameters characterising properties of hierarchical mergers, e.g. a value of  $\bar{\chi}_{\text{typ}}$  and  $m_{\text{crit},\mu}$  at the plateau, are more precisely constrained.

Finally, to investigate whether the bending point is robustly verified, we also fit the distribution by a straight line, i.e. assuming  $m_{\text{crit},\mu} \rightarrow \infty$  in Eq. (14), and calculate the Bayes factor of the model with broken lines (Eq. 14) compared to the model with a single line ( $m_{\text{crit},\mu} \rightarrow \infty$ ), where we set the likelihood function to Eq. (14) with the fitted parameters. For  $N_{\text{obs}} = 44$ , 100, and 1000, the logarithm of the Bayes factor is 0.0, 2.0, and 21, respectively. If we adopt the Akaike information criterion (Akaike 1974), the model with the broken lines is preferred by a factor of  $\sim 10^{1.5}$  for  $N_{\text{obs}} = 100$ , and the preference increases as  $N_{\text{obs}}$  increases. In the analysis using the observed data in § 3.2.1, although we assumed the existence of the plateau, the Bayes factors using the observed events (with  $D_{\text{KL,cri}} = 0, 0.05, 0.1$ , and  $0.15$ ) are in the range of  $10^{-0.1}-10^{0.1}$ , suggesting that the existence of the plateau is uncertain. Our analysis suggests that as the number of GW events increases to  $\gtrsim O(100)$ , the existence of the plateau can be confirmed with high significance.

#### 4. SUMMARY AND CONCLUSIONS

In this paper we have investigated characteristic distributions of  $\chi_{\text{eff}}$ ,  $\chi_{\text{p}}$ ,  $\chi_{\text{typ}} = (\chi_{\text{p}}^2 + \chi_{\text{eff}}^2)^{1/2}$ , and  $m_{\text{chirp}}$  expected from hierarchical mergers among stellar-mass BHs. We then used a toy model to derive the profile of the average of  $\chi_{\text{typ}}$  as a function of  $m_{\text{chirp}}$  for the events observed by LIGO/Virgo O1-O3a. We also investigated how well predictions in different models match observed spin and mass distributions by using Bayes factors. Finally, we estimate how well the  $\chi_{\text{typ}}$  profile can be recon-

structed using mock GW data expected in hierarchical mergers. Our main results are summarized as follows:

1. If hierarchical mergers are frequent, and the spin distribution of first-generation (1g) BHs does not strongly depend on their mass, the  $\bar{\chi}_{\text{typ}}$  profile as a function of  $m_{\text{chirp}}$  is characterized by a monotonic increase of  $\bar{\chi}_{\text{typ}}$  with  $m_{\text{chirp}}$  up to the maximum chirp mass among 1g BHs, and reaches a plateau of  $\bar{\chi}_{\text{typ}}$  with  $\sim 0.6$  at higher  $m_{\text{chirp}}$  (Fig. 1). With  $\sim 50$  events, the plateau and the rise of  $\chi_{\text{typ}}$  to 0.6 can be confirmed if the detection fraction of mergers of high-g BHs roughly exceeds  $\sim 0.5$  and  $\sim 0.15$ , respectively.
2. The maximum mass for 1g BHs can be estimated by constraining the transition point between the two regimes in the  $\bar{\chi}_{\text{typ}}$  profile. Also, the typical spin magnitude for 1g BHs is constrained from  $\bar{\chi}_{\text{typ}}$  at around minimum  $m_{\text{chirp}}$  among GW events.
3. The  $\bar{\chi}_{\text{typ}}$  profile reconstructed from the LIGO/Virgo O1-O3a data prefers a monotonic increase in  $\bar{\chi}_{\text{typ}}$  at  $m_{\text{chirp}} \lesssim 15-50 M_{\odot}$  with  $\sim 2\sigma$  confidence (Fig. 6), consistent with the evolution of BH spin magnitudes by hierarchical mergers. The maximum mass and the typical spin magnitude of 1g BHs are loosely constrained to be  $\sim 20-60 M_{\odot}$  and  $\lesssim 0.4$  with  $\sim 1\sigma$  credible intervals, respectively.
4. A Bayesian analysis using the  $\chi_{\text{eff}}$ ,  $\chi_{\text{p}}$ , and  $m_{\text{chirp}}$  distributions suggests that 1g BHs are preferred to have the maximum mass of  $m_{\text{max}} \sim 15-30 M_{\odot}$  if hierarchical mergers are frequent, which is consistent with mergers in AGN disks and/or nuclear star clusters. On the other hand, if mergers mainly originate from globular clusters (in which  $m_{\text{max}}$  is assumed to be  $45 M_{\odot}$ ), 1g BHs are favored to have spin magnitudes of  $\sim 0.3$ . These favored models are also consistent with the average and the standard deviation of  $\chi_{\text{p}}$  estimated in [The LIGO Scientific Collaboration et al. \(2020c\)](#).
5. By using observed data of more than  $\sim 100$  events in the future, we will be able to recover parameters characterizing the  $\bar{\chi}_{\text{typ}}$  distribution (e.g. the existence of the plateau and the value of  $\bar{\chi}_{\text{typ}}$  at the plateau  $b_{\mu}$ ) more precisely.

HT thank Davide Gerosa for providing us values for the Kullback-Leibler divergence, and Berry Christopher and Kengo Tomida for valuable comments. This work is financially supported by the Grant-in-Aid for JSPS Research Fellowship and for Basic Research by the Ministry of Education, Science and Culture of Japan (HT:17H01102, 17H06360, KO:17H02869, 17H01102, 17H06360). ZH acknowledges support from NASA grant NNX15AB19G and NSF grants 1715661 and 2006176. This work received funding from the European Research Council (ERC) under the European Union’s Horizon 2020 Programme for Research and Innovation ERC-2014-STG under grant agreement No. 638435 (GalNUC) (to BK). IB acknowledges support from the Alfred P. Sloan

Foundation and from the University of Florida. Simulations and analyses were carried out on Cray XC50 at the Center for Computational Astrophysics, National Astronomical Observatory of Japan.

## REFERENCES

Aasi, J., et al. 2015, *CQG*, **32**, 074001  
 Abbott, B. P., Abbott, R., Abbott, T. D., et al. 2019a, *ApJ*, **882**, L24  
 —. 2019b, *Physical Review X*, **9**, 031040  
 Abbott, R., Abbott, T. D., Abraham, S., et al. 2020a, *ApJ*, **896**, L44  
 —. 2020b, arXiv e-prints, arXiv:2010.14527  
 —. 2020c, *ApJ*, **900**, L13  
 Acernese, F., et al. 2015, *CQG*, **32**, 024001  
 Akaike, H. 1974, *IEEE Transactions on Automatic Control*, **19**, 716  
 Antonini, F., Gieles, M., & Gualandris, A. 2019, *MNRAS*, **486**, 5008  
 Antonini, F., Toonen, S., & Hamers, A. S. 2017, *ApJ*, **841**, 77  
 Apostolatos, T. A., Cutler, C., Sussman, G. J., & Thorne, K. S. 1994, *Phys. Rev. D*, **49**, 6274  
 Arca Sedda, M. 2020, arXiv e-prints, arXiv:2002.04037  
 Askar, A., Davies, M. B., & Church, R. P. 2020, arXiv e-prints, arXiv:2006.04922  
 Banerjee, S. 2017, *MNRAS*, **467**, 524  
 Bardeen, J. M., & Petterson, J. A. 1975, *ApJ*, **195**, L65  
 Bartos, I., Kocsis, B., Haiman, Z., & Márka, S. 2017, *ApJ*, **835**, 165  
 Baverá, S. S., Fragos, T., Qin, Y., et al. 2019, arXiv e-prints, arXiv:1906.12257  
 Belczynski, K., Daniel, E. H., Bulik, T., & O'Shaughnessy, R. 2016, *Nature*, **534**, 512  
 Bellovary, J. M., Mac Low, M.-M., McKernan, B., & Ford, K. E. S. 2016, *ApJ*, **819**, L17  
 Brodie, J. P., Romanowsky, A. J., Strader, J., et al. 2014, *ApJ*, **796**, 52  
 Buonanno, A., Kidder, L. E., & Lehner, L. 2008, *Phys. Rev. D*, **77**, 026004  
 Chen, H.-Y., Holz, D. E., Miller, J., et al. 2017, arXiv e-prints, arXiv:1709.08079  
 de Mink, S. E., & Mandel, I. 2016, *MNRAS*, **460**, 3545  
 Di Carlo, U. N., Giacobbo, N., Mapelli, M., et al. 2019, *MNRAS*, **487**, 2947  
 Do, T., Kerzendorf, W., Konopacky, Q., et al. 2018, *ApJ*, **855**, L5  
 Doctor, Z., Wysocki, D., O'Shaughnessy, R., Holz, D. E., & Farr, B. 2020, *ApJ*, **893**, 35  
 Dominik, M., Belczynski, K., Fryer, C., et al. 2012, *ApJ*, **759**, 52  
 Fishbach, M., & Holz, D. E. 2017, *ApJ*, **851**, L25  
 —. 2020, *ApJ*, **891**, L27  
 Fishbach, M., Holz, D. E., & Farr, B. 2017, *ApJ*, **840**, L24  
 Fishbach, M., Holz, D. E., & Farr, W. M. 2018, *ApJ*, **863**, L41  
 Fuller, J., & Ma, L. 2019, *ApJ*, **881**, L1  
 Gerosa, D., & Berti, E. 2017, *Phys. Rev. D*, **95**, 124046  
 Gerosa, D., Lima, A., Berti, E., et al. 2019, *Classical and Quantum Gravity*, **36**, 105003  
 Gerosa, D., Mould, M., Gangardt, D., et al. 2020a, arXiv e-prints, arXiv:2011.11948  
 Gerosa, D., Vitale, S., & Berti, E. 2020b, arXiv e-prints, arXiv:2005.04243  
 Gondán, L., Kocsis, B., Raffai, P., & Frei, Z. 2018, *ApJ*, **860**, 5  
 Hamers, A. S., & Safarzadeh, M. 2020, *ApJ*, **898**, 99  
 Hannam, M., Schmidt, P., Bohé, A., et al. 2014, *Phys. Rev. Lett.*, **113**, 151101  
 Hastings, W. K. 1970, *Biometrika*, **57**, 97  
 Hotokezaka, K., & Piran, T. 2017, *ApJ*, **842**, 111  
 Inayoshi, K., Hirai, R., Kinugawa, T., & Hotokezaka, K. 2017, *MNRAS*, **468**, 5020  
 Ivanova, N., Justham, S., Chen, X., et al. 2013, *The Astronomy and Astrophysics Review*, **21**, 59  
 Kalogera, V. 2000, *ApJ*, **541**, 319  
 Kesden, M., Sperhake, U., & Berti, E. 2010, *Phys. Rev. D*, **81**, 084054  
 Kidder, L. E. 1995, *Phys. Rev. D*, **52**, 821  
 Kimball, C., Talbot, C., Berry, C. P. L., et al. 2020a, *ApJ*, **900**, 177  
 —. 2020b, arXiv e-prints, arXiv:2011.05332  
 Kinugawa, T., Inayoshi, K., Hotokezaka, K., Nakauchi, D., & T., N. 2014, *MNRAS*, **442**, 2963  
 Kocsis, B., Yunes, N., & Loeb, A. 2011, *Phys. Rev. D*, **84**, 024032  
 Kumamoto, J., Fujii, M. S., & Tanikawa, A. 2018, arXiv e-prints, arXiv:1811.06726  
 Leaman, R., VandenBerg, D. A., & Mendel, J. T. 2013, *MNRAS*, **436**, 122  
 Liu, B., & Lai, D. 2020, arXiv e-prints, arXiv:2009.10068  
 Lubow, S. H., Seibert, M., & Artymowicz, P. 1999, *ApJ*, **526**, 1001  
 Mandel, I., & de Mink, S. E. 2016, *MNRAS*, **458**, 2634  
 Mandel, I., Farr, W. M., & Gair, J. R. 2019, *MNRAS*, **486**, 1086  
 Mapelli, M., Santoliquido, F., Bouffanais, Y., et al. 2020, arXiv e-prints, arXiv:2007.15022  
 Marchant, P., Langer, N., Podsiadlowski, P., Tauris, T., & Moriya, T. 2016, *A&A*, **588**, A50  
 McKernan, B., Ford, K. E. S., & O'Shaughnessy, R. 2020a, *MNRAS*, **498**, 4088  
 McKernan, B., Ford, K. E. S., O'Shaughnessy, R., & Wysocki, D. 2020b, *MNRAS*, **494**, 1203  
 McKernan, B., Ford, K. E. S., Bellovary, J., et al. 2018, *ApJ*, **866**, 66  
 Michaela, E., & Perets, H. B. 2019, *ApJ*, **887**, L36  
 Moody, M. S. L., Shi, J.-M., & Stone, J. M. 2019, arXiv e-prints, arXiv:1903.00008  
 O'Leary, R. M., Kocsis, B., & Loeb, A. 2009, *MNRAS*, **395**, 2127  
 O'Leary, R. M., Meiron, Y., & Kocsis, B. 2016, *ApJL*, **824**, L12  
 Olejak, A., Fishbach, M., Belczynski, K., et al. 2020, *ApJ*, **901**, L39  
 Paczynski, B. 1976, in *IAU Symposium, Structure and Evolution of Close Binary Systems*, **73**, 75  
 Pan, Z., & Yang, H. 2021, arXiv e-prints, arXiv:2101.09146  
 Pavlovskii, K., Ivanova, N., Belczynski, K., & Van, K. X. 2017, *MNRAS*, **465**, 2092  
 Peng, E. W., Jordán, A., Côté, P., et al. 2006, *ApJ*, **639**, 95  
 Planck Collaboration, Ade, P. A. R., Aghanim, N., et al. 2016, *A&A*, **594**, A13  
 Portegies Zwart, S. F., & McMillan, S. L. W. 2000, *ApJ*, **528**, L17  
 Pratten, G., Schmidt, P., Buscicchio, R., & Thomas, L. M. 2020, *Physical Review Research*, **2**, 043096  
 Rasskazov, A., & Kocsis, B. 2019, arXiv e-prints, arXiv:1902.03242  
 Rastello, S., Amaro-Seoane, P., Arca-Sedda, M., et al. 2019, *MNRAS*, **483**, 1233  
 Rastello, S., Mapelli, M., Di Carlo, U. N., et al. 2020, *MNRAS*, **497**, 1563  
 Rodriguez, C. L., Amaro-Seoane, P., Chatterjee, S., & Rasio, F. A. 2018, *Phys. Rev. Lett.*, **120**, 151101  
 Rodriguez, C. L., Chatterjee, S., & Rasio, F. A. 2016a, *Phys. Rev. D*, **93**, 084029  
 Rodriguez, C. L., Zevin, M., Amaro-Seoane, P., et al. 2019, *Phys. Rev. D*, **100**, 043027  
 Rodriguez, C. L., Zevin, M., Pankow, C., Kalogera, V., & Rasio, F. A. 2016b, *ApJ*, **832**, L2  
 Rodriguez, C. L., Kremer, K., Grudić, M. Y., et al. 2020, *ApJ*, **896**, L10  
 Safarzadeh, M., Farr, W. M., & Ramirez-Ruiz, E. 2020a, arXiv e-prints, arXiv:2001.06490  
 Safarzadeh, M., & Haiman, Z. 2020, arXiv e-prints, arXiv:2009.09320  
 Safarzadeh, M., Hamers, A. S., Loeb, A., & Berger, E. 2020b, *ApJ*, **888**, L3  
 Samsing, J., MacLeod, M., & Ramirez-Ruiz, E. 2014, *ApJ*, **784**, 71  
 Samsing, J., Bartos, I., D'Orazio, D. J., et al. 2020, arXiv e-prints, arXiv:2010.09765  
 Schmidt, P., Ohme, F., & Hannam, M. 2015, *Phys. Rev. D*, **91**, 024043  
 Schödel, R., Nogueras-Lara, F., Gallego-Cano, E., et al. 2020, arXiv e-prints, arXiv:2007.15950  
 Scott, D. 1992, *Multivariate Density Estimation: Theory, Practice, and Visualization*, A Wiley-interscience publication (Wiley)  
 Silsbee, K., & Tremaine, S. 2017, *ApJ*, **836**, 39  
 Spera, M., Mapelli, M., Giacobbo, N., et al. 2019, *MNRAS*, **485**, 889  
 Stone, N. C., Metzger, B. D., & Haiman, Z. 2017, *MNRAS*, **464**, 946  
 Tagawa, H., Haiman, Z., Bartos, I., & Kocsis, B. 2020a, *ApJ*, **899**, 26  
 Tagawa, H., Haiman, Z., & Kocsis, B. 2020b, *ApJ*, **898**, 25  
 Tagawa, H., Kocsis, B., Haiman, Z., et al. 2021a, *ApJ*, **907**, L20  
 —. 2021b, *ApJ*, **908**, 194  
 Tagawa, H., Kocsis, B., & Saitoh, R. T. 2018, *Phys. Rev. Lett.*, **120**, 261101  
 The LIGO Scientific Collaboration, the Virgo Collaboration, Abbott, B. P., et al. 2019, arXiv e-prints, arXiv:1906.08000  
 The LIGO Scientific Collaboration, the Virgo Collaboration, Abbott, R., et al. 2020a, arXiv e-prints, arXiv:2004.08342  
 —. 2020b, arXiv e-prints, arXiv:2009.01075  
 —. 2020c, arXiv e-prints, arXiv:2010.14533  
 Tiwari, V., & Fairhurst, S. 2020, arXiv e-prints, arXiv:2011.04502  
 van den Heuvel, E. P. J., Portegies Zwart, S. F., & de Mink, S. E. 2017, *MNRAS*, **471**, 4256  
 Veitch, J., Raymond, V., Farr, B., et al. 2015, *Phys. Rev. D*, **91**, 042003

Venumadhav, T., Zackay, B., Roulet, J., Dai, L., & Zaldarriaga, M. 2019, arXiv e-prints, arXiv:1904.07214

Vitale, S., Gerosa, D., Farr, W. M., & Taylor, S. R. 2020, arXiv e-prints, arXiv:2007.05579

Yang, Y., Bartos, I., Haiman, Z., et al. 2020a, arXiv e-prints, arXiv:2003.08564

Yang, Y., Gayathri, V., Bartos, I., et al. 2020b, arXiv e-prints, arXiv:2007.04781

Yang, Y., Bartos, I., Gayathri, V., et al. 2019, *Phys. Rev. Lett.*, **123**, 181101

Zackay, B., Dai, L., Venumadhav, T., Roulet, J., & Zaldarriaga, M. 2019, arXiv e-prints, arXiv:1910.09528

Zevin, M., Spera, M., Berry, C. P. L., & Kalogera, V. 2020a, *ApJ*, **899**, L1

Zevin, M., Bavera, S. S., Berry, C. P. L., et al. 2020b, arXiv e-prints, arXiv:2011.10057

Ziosi, B. M., Mapelli, M., Branchesi, M., & Tormen, G. 2014, *MNRAS*, **441**, 3703